Title

Part 1: The Effect of Lattice Defects on the Sintering of Lithium Fluoride. Part 2: The Morphology of Calcium Oxide from Calcium Carbonate Decomposition

Author

Fenwick, D.M.

Publication Date

1990-09-01

LBL-28303

Lawrence Berkeley Laboratory
UNIVERSITY OF CALIFORNIA

Materials & Chemical Sciences Division

Part 1: The Effect of Lattice Defects on the Sintering of Lithium Fluoride

Part 2: The Morphology of Calcium Oxide from Calcium Carbonate Decomposition

D.M. Fenwick
(M.S. Thesis)

September 1990

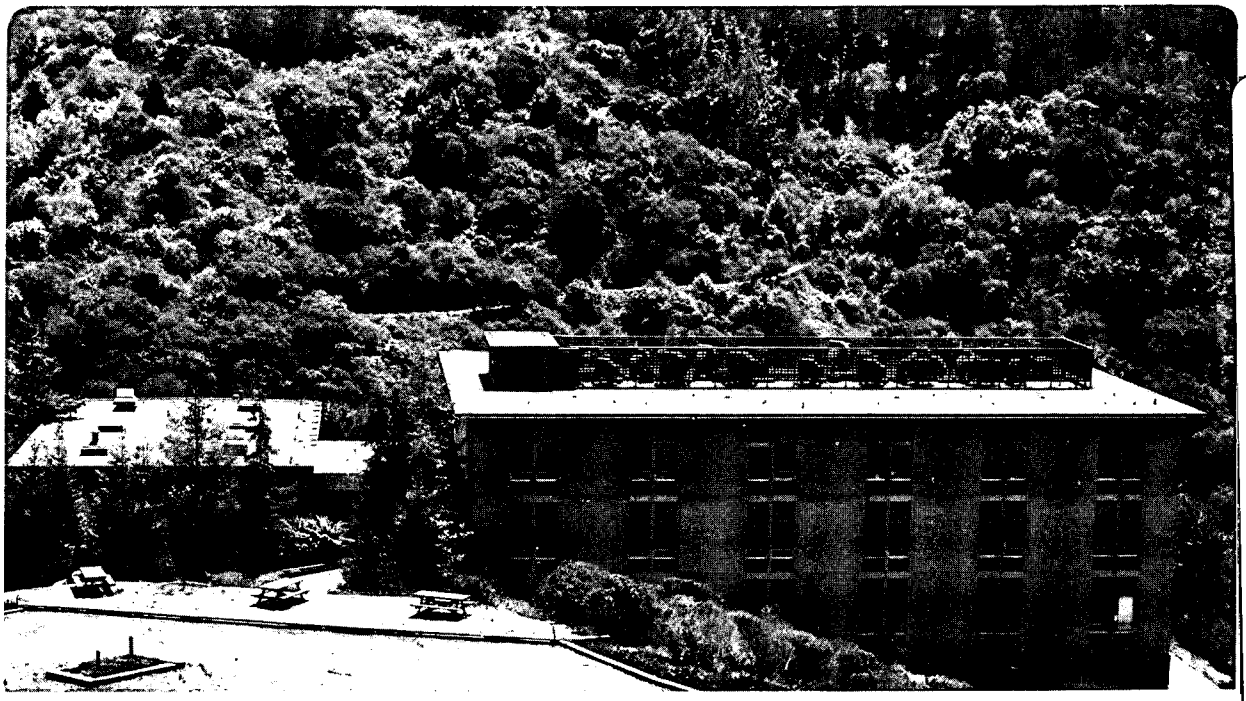

Prepared for the U.S. Department of Energy under Contract Number DE-AC03-76SF00098.

DISCLAIMER

LBL-28303

PART 1

THE EFFECT OF LATTICE DEFECTS ON THE SINTERING OF LITHIUM FLUORIDE

PART 2

THE MORPHOLOGY OF CALCIUM OXIDE FROM CALCIUM CARBONATE DECOMPOSITION

David M. Fenwick

Master of Science Thesis

September 1990

Materials Science Division
Lawrence Berkeley Laboratory
and Department of Materials Science and Mineral Engineering
University of California
Berkeley, California 94720

This work was supported by the Director, Office of Energy Research, Office of Basic Energy Science, Materials Sciences Division of the U.S. Department of Energy under Contract Number DE-AC03-76SF00098.

Table of Contents

PREFACE

This thesis is divided into two unrelated parts. Part 1 discusses a study in which a theory of surface melting of solids was tested. A series of experiments failed to prove this theory. As a result, a study of the morphology of CaO produced from $CaCO_3$ decomposition was initiated. The second study is discussed in Part 2.

PART 1:

THE EFFECT OF LATTICE DEFECTS ON THE SINTERING OF LITHIUM FLUORIDE

Introduction

Our motivation for studying the effect of lattice defects on sintering kinetics came from a theory by Searcy concerning surface melting of solids[1]. Surface melting has been shown to occur in ice[2], argon[3], and lead[4] at temperatures below the melting point. While surface melting of this sort is an equilibrium phenomenon, Searcy has predicted that surface melting may also occur in a non-equilibrium situation--when a solid is being rapidly heated and has a below-equilibrium concentration of vacancies for the temperature reached. If the surfaces of powders within a powder compact melted while it was being heated, its densification rate might exceed the expected value for a given temperature, because the atomic flux within and along the liquid layer could be comparable to fluxes in liquid phase assisted sintering.

According to Searcy's hypothesis, melting below the equilibrium fusion point could occur if a solid has a vacancy concentration lower than the equilibrium value because the thermodynamic activity of a solid varies inversely with its vacancy concentration. This conclusion follows from[5]

$$G_b^t - G_{v_b}^t + RT\ln(X_b/X_{v_b}) = \mu_{(solid)}. \qquad (1)$$

G_b^t is the molar thermal free energy of atoms in the bulk material, $G_{v_b}^t$ is the molar thermal free energy of formation of vacancies in the bulk material, X_b is the fraction

of lattice sites occupied by atoms, X_{vb} is the fraction of lattice sites occupied by vacancies, and $\mu_{(solid)}$ is the chemical potential or molar free energy of the solid component. Equation (1) was derived from kinetic relations by assuming the exchange of vacancies and atoms reaches equilibrium within all sub-parts of a crystal, including the self-adsorption layer, and between the self-adsorption layer and the gas. The equation also has been derived by minimizing the free energy for atom-vacancy exchange under the constraints that the total number of atom and vacancy sites is constant.[5]

If we let $\mu_v = G_{vb}^{f} + RT\ln X_{vb}$ then equation (1) becomes the expression first developed by Herring:[6]

$$\mu_{(solid)} = \mu_{(bulk\ atoms)} - \mu_v. \tag{2}$$

The difference between the chemical potential of a solid with an arbitrary vacancy concentration and that of the solid with its equilibrium vacancy concentration would be

$$\mu_{(solid)} - \mu^{o}_{(solid)} = (\mu_{(bulk\ atoms)} - \mu_v) - (\mu^{o}_{(bulk\ atoms)} - \mu^{o}_v)$$

$$\cong \mu^{o}_v - \mu_v. \tag{3}$$

But

$$\mu^{o}_v - \mu_v = RT\ln(X^{o}_v / X_v). \tag{4}$$

Combining equations (3) and (4) gives

$$\mu_{(solid)} - \mu^{o}_{(solid)} \cong RT\ln(X^{o}_v / X_v), \tag{5}$$

or

$$a_{(solid)} = X^{o}_v / X_v \tag{6}$$

where $a_{(solid)}$ is the thermodynamic activity of the solid relative to its activity in its standard state in which an equilibrium concentration of vacancies is present. It is well established that higher than equilibrium defect concentrations destabilize a solid.[7,8] Equation (6) predicts that its activity should also vary inversely with decreases in vacancy concentrations below the equilibrium value. When a crystal has an equilibrium concentration of vacancies $X_{vb} = \exp(-G_{vb}^{f}/kT)$, and equation (1) reduces to the accepted expression

$$G_b^f + RT\ln X_b = \mu_{(bulk\ atoms)} = \mu_{(solid)}. \qquad (7)$$

Equation (1) or (6) would only apply when a crystal is in dynamic equilibrium with the gaseous phase. However, dynamic equilibrium between the solid and gas would exist within a relatively large powder compact containing relatively small particles, since the equilibrium vapor pressure is established within such compacts.[9] Thus if a powder compact were heated rapidly enough, so that the vacancy concentration lagged well behind the equilibrium value, the chemical potential could exceed that for the liquid phase; the material would then be unstable with respect to melting. It has been established that melting nucleates at surfaces and that superheating at a surface would be unlikely.[10] Once a particle surface became liquid or amorphous equation (1) or (6) would no longer apply and re-solidification to produce a solid with an equilibrium vacancy concentration could occur. Re-melting could again occur if further heating caused the vacancy concentration to again lag behind the equilibrium values for the higher temperatures reached. The cycle could continue as long as the temperature continued to increase until the equilibrium melting temperature was reached. Such a process could explain the fact that powder compacts such as alumina[11-13], zinc oxide[14], and alumina-titanium carbide composites[15] have been

shown to reach densities during rapid heating that depend primarily on the temperature reached, since a liquid layer could begin to form at lower temperatures for faster heating rates. However, a different model attributes the relative independence of density increases on heating rates to high coarsening rates.[14] That model shows that the density changes of zinc oxide powder compacts, which undergo a significant amount of coarsening during sintering, have a weak dependence on the constant heating rate α over a wide density range:

$$\Delta\rho \sim \alpha^{-1/2} F(T)\Phi(\rho) \tag{8}$$

where $F(T)$ is a function of temperature only and $\Phi(\rho)$ is a function of density only. The value of -1/2 for the exponent of α was obtained by assuming that volume diffusion is the dominant densifying mechanism for ZnO. If grain boundary diffusion is the dominant densifying mechanism, this value is closer to zero, and the density change is nearly independent of the heating rate.

To test the surface melting theory we have compared the density changes of two different types of powder compacts of lithium fluoride after subjecting both to the same fast-firing heat treatment. One type of compact consisted of powder originating from a crystal which we had quenched from a high temperature, and the other consisted of powder from a crystal which we had annealed at a lower temperature. Studies on the quenching of CaF_2 have shown that the dislocation density is much higher in quenched samples than in slowly cooled samples.[16] Thus the powder from quenched crystals should have had a higher concentration of lattice defects than the powder from annealed crystals before the compacts were heated. Searcy hypothesized that the powder with the higher concentration of lattice defects might densify less, despite being less stable than the annealed powder before heating was begun. The reason is that

during rapid heating pre-existing vacancies and a high dislocation density would provide vacancy concentrations closer to the equilibrium values at higher temperatures. As a result, the powder with the higher defect concentration would have a lower activity and be less likely to undergo surface melting; its surface diffusion rates would then be less than those of the other type of powder, whose surfaces would melt. Hence the compact containing the powder with quenched-in defects would densify less rapidly than the other one.

The Experiment

One set of LiF crystals[a] was pushed from an 800-830 °C hot zone in an alumina-tube furnace into room-temperature air or water. Another set of crystals was annealed for ~ 4 h at ~ 550 °C and then allowed to cool ~ 5 °C/min in the furnace. Since the melting point of LiF is 847 °C, annealing at 550 °C should have been sufficient to anneal out many of the ~ 10^6 cm^{-2} dislocations[17] typically found in melt-grown LiF crystals. If the LiF crystals had at least 80 ppm of divalent impurities, the concentration of point defects in the crystals quenched from 800 °C would not have been significantly different from the point defect concentration in the annealed crystals.[18] Since the quenched crystals were subjected to much greater thermal stresses, however, they should have had a much greater concentration of dislocations[b], which would act as vacancy sources on reheating. All crystals were wrapped in platinum foil, which was exposed to air, during the heat treatments. There should have been no significant

a. These were Optovac melt-grown crystals made from zone-refined starting material.
b. Slip lines were visible when the LiF was quenched into water, and the crystals often fractured.

contamination of LiF from the air, since LiF is stable with respect to oxygen, nitrogen, hydrogen, and water. Any visible contamination of the crystal surfaces from the furnace tube was cleaned off with tetrafluoroboric acid and acetone.

The two sets of crystals were ground separately in an alumina mortar. They were usually ground within liquid nitrogen, which should have reduced the number of defects introduced through grinding by lowering the temperature of the LiF to a point where it was less ductile. However, in some cases the quenched crystals were first ground in air and then in liquid nitrogen, a procedure which may have introduced many more defects into that material (as desired). In this case grinding in liquid nitrogen was done to ensure that the surfaces of the powder from quenched crystals had chemical characteristics similar to those of the surfaces of powder from annealed crystals (e.g. the same amount of water adsorbed). In other cases both sets of crystals were ground in air alone. The powder from both sets of crystals was allowed to dry (if necessary) and then sifted through a 45 μm (325 mesh) sieve.

The seived powders produced from the annealed and quenched LiF were next formed into pellets. Each pellet was made by placing about 0.5 grams of the powder into a 3/8-inch diameter stainless steel die coated with stearic acid. The die was placed within a hydraulic press and subjected to a pressure of ~ 49 MPa. Apparent densities were calculated from the sample weight and dimensions. A microbalance was used to weigh the material, and a micrometer was used to measure the pellet dimensions. Most of the pellets had relative densities of ~ 71 ± 2 %.

One pellet of each type was then placed on platinum foil within a 3 cm diameter quartz tube. The pellets were lined up perpendicular to the long axis of the quartz tube, as shown in Figure 1. Both pellets were approximately the same size and had

approximately the same densities. The quartz tube was attached to a device which could be moved on rollers to and from a furnace (see Figure 1). The tip of a chromel-alumel thermocouple was placed near the center of the furnace. The inner diameter of the furnace was ~ 15 mm, and its inner length was ~ 70 mm. When the furnace reached about 910 ^{o}C the tube was rolled into the furnace and removed after 160 - 195 s. The surfaces of the pellets would begin to melt if they were left in the furnace for more than 195 s, and they would completely melt after ~ 230 s. These observations imply that the heating rate was ~ 4 ^{o}C/s for the pellet surfaces and ~ 3.7 ^{o}C/s for the centers of the pellets. In some cases, however, the furnace temperature was only 890 ^{o}C, and the heating rate was lower. Since the furnace was large and the pellets were lined up at the same point on the axis along which the tube was moved, both pellets received about the same heat treatment.

After each pair of pellets was subjected to fast-firing their dimensions and weight were measured again, and their final densities were calculated. The major source of error in dimension measurements was the fact that some of the pellets were slightly warped after firing. The warping usually was not visible, however, being only detectable with a micrometer. The pellet surfaces had minor irregularities (see Figures 2 and 3). Repeated measurements on a slightly warped pellet indicated that the relative density measurements were reproducible to within ± 0.003.

The entire experimental procedure was repeated several times and the density changes of many different pairs of pellets were measured (tables 1 to 5). To obtain an estimate of the impurity concentration within the LiF, some of the LiF crystals were analyzed by atomic emission spectroscopy.

Results and Discussion

Tables 1 to 5 list the characteristics of each pellet and its density change after fast-firing. Each row contains all the relevant data for one pellet. The heat treatment given to a certain set of LiF crystals is indicated in the left-most column of each row. Here "A" stands for annealing, and "Q" stands for quenching in air (unless otherwise specified). In the next column is the fraction of powder, made from that set of crystals, which passed through the sieve and was used to make the pellet. The number of seconds the pellet was placed in the furnace is listed in the third column. The pre-firing and post-firing densities for the pellet are given in the next two columns. Densities are given as fractions of the maximum theoretical density. The density change for the pellet is shown in the fifth column. The results are grouped in pairs for comparison of the pellets which were placed in the furnace together. Each block of results delineated by the solid lines represents data from one complete experimental procedure, as described in the previous section.

The microstructure of a representative sample after compaction is shown in Figure 4. A fast-fired sample is shown in Figure 5. The furnace temperature was 910 ^{o}C in all cases except for the Table 1 experiments, in which the temperature was 890 ^{o}C.

Table 1 lists data for pellets made from crystals which were ground in air alone. As can be seen in the second column from the left, about the same fraction of powder from the annealed and quenched crystals passed through the sieve; hence, if the particle size distributions were similar the average size of the particles from both sets of crystals should have also been similar. The green densities of the pellets were quite high--near 80 %--resulting from a high compaction pressure of ~ 189 MPa. In order to minimize

the number of defects introduced during compaction, less pressure (~ 49 MPa) was used to make the pellets in subsequent experiments, the results of which are given in Tables 2 to 5. This pressure still exceeded the room-temperature elastic limit for LiF single crystals (12.7 MPa)[19]; dislocations must have been generated during compaction in all the experiments. The high green densities (~ 70 %) also suggest that the compacts were deformed during pressing. Unfortunately, the pellets would usually crumble during handling if a compaction pressure less than 49 MPa was applied.

The last column in Table 1 shows that in each case the density changes of the two pellets placed in the furnace together were approximately equal. This result is not what was predicted by Searcy's model, but it is not surprising given that the average particle sizes and green densities for both pellets were approximately equal. The differences in densification among different *pairs* of pellets are primarily due to differences in the length of time they were placed in the furnace.

The data of Table 1 show that there is no systematic difference between the density increases of annealed and quenched samples. A possible reason for this result is that in both quenched and annealed samples similar high defect concentrations were introduced during grinding of the crystals after their heat treatments. In order to minimize the number of defects introduced through grinding, LiF crystals were ground in liquid nitrogen in subsequent experiments.

Table 2 contains the data for pellets made from crystals which were ground in liquid nitrogen. The measured density increases for the compacts prepared from annealed LiF crystals were greater than those of compacts prepared from quenched crystals in all but one experiment. However, many of the density change differences were within the range of experimental error (± .003). Furthermore, in the first and

last block of results, the compacts prepared from annealed crystals probably had smaller average particle sizes, since a greater fraction of powder from the annealed crystals passed through the sieve. Pellets having a smaller average particle size are expected to densify more. The data of Table 2, therefore, do not prove a systematic dependence of densification on the heat treatments. The green densities of the pellets placed in the furnace together were nearly equal and, in the range used, appear to have no significant effect on the density changes.

Table 3 lists results from an experiment in which the annealed crystals were subjected to the same heat treatment as in the previous experiments (~ 4 hours at 550 ^{o}C), but the other set of crystals was quenched in water rather than air. Both sets of crystals were then ground in liquid nitrogen. Quenching in water produced many more dislocations in the crystals than quenching in air; slip lines were visible only when crystals were quenched in water. The right-most column shows that there was no significant difference between the density changes of the compacts prepared from water-quenched and annealed LiF. Because both types of compacts probably had similar average particle sizes, these results imply that the heat treatments had no significant effect on sintering kinetics.

Another method was used to (possibly) introduce a high concentration of lattice defects into the quenched LiF crystals relative to the defect concentration in the annealed crystals. In most cases the crystals were quenched in air, but in some experiments they were quenched in water. The quenched crystals were first ground in air and then in liquid nitrogen. The annealed crystals were ground only in liquid nitrogen. Despite the different grinding techniques and heat treatments, however, no significant effect of lattice defects on sintering kinetics was found (see Table 4). Most

of the density change differences were within the range of experimental error, although in the second block of results the compacts with the much higher "% through sieve" value had consistently higher measured density increases. In two runs marked with asterisks the powder compact prepared from annealed LiF densified less than the corresponding samples from water-quenched LiF despite the probable smaller average particle size of the annealed samples.

To clarify the effect of particle size on density changes, we compared the density changes of pellets with different average particle sizes that were made from LiF crystals subjected to the same heat treatment. All of the crystals had been annealed together at 550 ^{o}C for ~ 4 h, but one set of these crystals was ground for a longer period of time than the other to create two sets of powder (and pellets) with different particle size distributions. 31 % of the powder that was ground longer passed through the sieve, compared to 26 % for the other set of powder. As shown in Table 5, in each case the density change was greater for the pellet with the smaller average particle size or "31% through sieve" value, although for the first two runs the density change differences were within the range of experimental error. Since these density change differences were comparable to those found in previous experiments (Tables 1 - 4), the results of this experiment support the conclusion that the difference between the density changes of the two types of pellets was primarily caused by their having different average particle sizes. This effect was most pronounced when the pellets were allowed to densify to a greater extent (see the first block of results in Table 2 and last pair of results in Table 5). As in previous experiments, the pre-sintered pellet densities listed in Table 5 were nearly equal and appear to not significantly affect the results.

There are many possible reasons why the quenching and annealing heat treatments had no measurable effect on the density changes of the powder compacts. The grinding and compaction processes which followed the heat treatments may have introduced so many defects into the LiF that there was no significant difference between the defect concentrations in powders from both quenched and annealed crystals. In addition, extrinsic vacancy concentrations in impure LiF crystals could have been high enough to prevent the activity of the solid from exceeding that of the liquid phase, thus preventing surface melting.

To obtain an estimate of the impurity concentration in the LiF, samples of the LiF crystals were analyzed by atomic emission spectroscopy. Impurity concentration detection limits for the 45 elements scanned by this technique are listed in Table 6. No impurities were detected; hence, most of the impurity concentrations within the LiF were probably well below the detection limits. Some of the detection limits were quite high (e.g., 1000 ppm for phosphorous), but magnesium tends to be the most prevalent element in zone-refined LiF, and the detection limit for magnesium is very low (10 ppm). However, even a relatively low total aliovalent impurity concentration (on the order of 100 ppm) would create vacancy concentrations comparable to the intrinsic vacancy concentration of LiF near its melting point.[18]

Another possible problem is that vacancies equilibrated within both types of powder too rapidly for a liquid layer to form on the powder surfaces. In fact, vacancies might equilibrate too rapidly for surface melting to occur in most solids, even if they are heated very rapidly.

The rate of vacancy equilibration in gold has been studied by Seidman and Balluffi.[20] They found that, when gold with a dislocation density of 10^7 cm^{-2} is rapidly

heated from 436 °C to 653 °C (61 % of its melting point) and held at that temperature, the equilibrium vacancy concentration is reached within ~ 1 s. Furthermore, when the gold is rapidly heated from 631 °C to 878 °C (83 % of its melting point) and held there, the equilibrium vacancy concentration is reached within ~ 0.2 s. Melt-grown LiF crystals typically have dislocation densities of ~ 10^6 cm^{-2}.[17] If equilibration rates are comparable in LiF to those in gold, near-equilibrium vacancy concentrations would be expected to be established during the heating of powders from both quenched and annealed crystals.

To estimate the vacancy equilibration rate in LiF, consider the average maximum diffusion distance for vacancies in gold and LiF with dislocation densities of 10^7 cm^{-2} and 10^6 cm^{-2}, respectively. This distance is equivalent to the average distance between dislocations, which is 3×10^{-4} cm for the gold and 1×10^{-3} cm for the LiF. When both materials are at the same temperature relative to their melting points, the value of the vacancy diffusion coefficients for both materials should be similar (see references (20) and (21) for comparisons of the enthalpy and entropies of migration of vacancies in gold and LiF). Hence, if the LiF is rapidly heated to 83 % of its melting point and held there, the time $t_{(LiF)}$ in which its vacancy concentrations would reach their equilibrium value could be estimated by letting

$$t_{(LiF)} = (X_{(LiF)} / X_{(gold)})^2 t_{(gold)} \tag{9}$$

where $X_{(LiF)}$ is the average distance between dislocations in the LiF, $X_{(gold)}$ is the average distance between dislocations in the gold, and $t_{(gold)}$ is the time in which vacancies equilibrated in the gold when it was rapidly heated to 83 % of its melting point (~ 0.2 s). The result is $t_{(LiF)} \cong 2$ s, one order of magnitude greater than the time for vacancy equilibration in the gold.

Surface melting certainly could occur within 2 s, but this result only applies to vacancy equilibration 10^{-3} cm from a vacancy source. For surface melting to occur, below-equilibrium vacancy concentrations probably would be required within 10 - 100 angstroms from a surface. According to equation (9), vacancy equilibration could occur within 10^{-7} - 10^{-6} s at distances this close to a surface (assuming $t_{(gold)}$ = 0.2 s and $X_{(gold)}$ = 10^{-4} cm^{-2}). Hence, a liquid layer would have to be able to form in less than 10^{-7} - 10^{-6} s. It is possible that a liquid layer could form within this time, since atoms in solids vibrate at frequencies of ~ 10^{13} s^{-1}. Nevertheless, it is important to note that the surfaces of the LiF powder compacts were heated at a rate of only ~ 4 ^{o}C/s, and the centers of the compacts were heated at a rate of only ~ 3.7 ^{o}C/s. In light of the study of vacancy generation in gold, these slow heating rates imply that at higher temperatures the vacancy concentrations would be very near their equilibrium values.

Conclusions

Comparisons of the density changes of the pairs of pellets placed in the furnace together show no significant difference between the density changes of pellets made from annealed crystals and those of pellets made from quenched crystals. There are many possible reasons for this result:

1) The powder surfaces did not melt during rapid heating. There may be no inverse relation between the thermodynamic activity of a solid and its vacancy concentration, or vacancies may have equilibrated too rapidly for surface melting to occur. Another possibility is that the extrinsic vacancy concentrations in the LiF were high enough to prevent the activity of the solid from exceeding that of the liquid phase. If this is true,

it is highly unlikely that surface melting could occur in commercially important powder compacts, because they would usually have higher concentrations of impurities than the LiF used in this study.

2) Surface melting did occur, but the extent to which it did in both types of pellets was negligible; surface or grain boundary diffusion rates were not affected significantly.

3) Surface melting occurred in all the pellets and atomic diffusion rates increased above their expected value for a given temperature, but the extent to which they increased was about equal for both types of pellets. The grinding and compaction processes may have introduced so many defects into both the quenched and annealed material that there was no significant difference in their defect concentrations. This would mean that the vacancy equilibration kinetics within both types of material were nearly the same despite the different heat treatments; hence, if surface melting occurred, the amount of surface melting and the diffusion rates within both types of pellets would have been approximately equal.

If the grinding process could have been better controlled so that the average particle sizes for each pellet would be nearly equal, perhaps some clear though small difference in densification might have been found. However, it would have been difficult to rule out other possibilities leading to small differences in densification behavior--such as slight differences in contamination of LiF from the heat treatments or differences between the fracture behavior of the quenched and annealed crystals leading to slightly different powder shapes. The only clear trend the experimental results show is the effect of particle size--smaller particle sizes enhance sintering kinetics, a well-known phenomenon.

Table 1 LiF Ground in Air

Heat Treatment	% Through Sieve	Seconds in Furnace	Green Density	Final Density	Density Change
A	39	150	.813	.823	.010
Q	40	150	.814	.828	.014
A	39	165	.813	.831	.018
Q	40	165	.814	.829	.015
A	39	195	.815	.845	.030
Q	40	195	.812	.842	.030
A	39	205	.814	.850	.036
Q	40	205	.811	.849	.038
A	40	180	.800	.820	.020
Q	40	180	.800	.816	.016
A	40	190	.806	.832	.026
Q	40	190	.802	.827	.025
A	40	200	.789	.815	.026
Q	40	200	.792	.819	.027
A	40	200	.775	.802	.027
Q	40	200	.773	.800	.027

Table 2 LiF Ground in Liquid Nitrogen

Heat Treatment	% Through Sieve	Seconds in Furnace	Green Density	Final Density	Density Change
A	19	180	.742	.790	.048
Q	16	180	.739	.765	.026
A	19	180	.744	.795	.051
Q	16	180	.745	.765	.020

Table 2 LiF Ground in Liquid Nitrogen

Heat Treatment	% Through Sieve	Seconds in Furnace	Green Density	Final Density	Density Change
A	19	180	.725	.789	.064
Q	16	180	.728	.753	.025
A	15	165	.725	.740	.015
Q	17	165	.726	.740	.014
A	15	165	.724	.743	.019
Q	17	165	.722	.735	.013
A	15	180	.723	.757	.034
Q	17	180	.722	.763	.041
A	27	165	.730	.759	.029
Q	29	165	.726	.748	.022
A	27	175	.728	.765	.037
Q	29	175	.728	.764	.036
A	27	180	.730	.775	.045
Q	29	180	.733	.772	.039
A	40	160	.715	.730	.015
Q	37	160	.716	.729	.013
A	40	160	.718	.730	.012
Q	37	160	.713	.720	.007
A	40	160	.719	.729	.010
Q	37	160	.716	.719	.003
A	40	160	.722	.738	.016
Q	37	160	.717	.722	.005
A	40	160	.717	.726	.009
Q	37	160	.711	.715	.004

Table 3 LiF Ground in Liquid Nitrogen

Heat Treatment	% Through Sieve	Seconds in Furnace	Green Density	Final Density	Density Change
A	35	165	.732	.762	.030
Q+	33	165	.726	.761	.035
A	35	165	.731	.760	.029
Q+	33	165	.732	.762	.030
A	35	170	.729	.775	.046
Q+	33	170	.728	.771	.043

+ quenched in water

Table 4 Quenched LiF Ground in Air, then Liquid Nitrogen
Annealed LiF Ground in Liquid Nitrogen

Heat Treatment	% Through Sieve	Seconds in Furnace	Green Density	Final Density	Density Change
A	29	170	.721	.760	.039
Q	34	170	.718	.762	.044
A	29	170	.720	.759	.039
Q	34	170	.715	.755	.040
A	29	170	.725	.765	.040
Q	34	170	.724	.764	.040
A	30	165	.707	.732	.025
Q	39	165	.708	.738	.030
A	30	170	.704	.740	.036
Q	39	170	.707	.747	.040
A	30	170	.697	.737	.040
Q	39	170	.697	.740	.043

Table 4 Quenched LiF Ground in Air, then Liquid Nitrogen
Annealed LiF Ground in Liquid Nitrogen

Heat Treatment	% Through Sieve	Seconds in Furnace	Green Density	Final Density	Density Change
A	30	170	.697	.741	.044
Q	39	170	.708	.757	.049
A	29	165	.693	.715	.022
Q	32	165	.701	.724	.023
A	29	165	.702	.727	.023
Q	32	165	.699	.731	.032
A	29	165	.700	.726	.026
Q	32	165	.707	.732	.025
A	29	165	.704	.731	.027
Q	32	165	.708	.735	.027
A	34	165	.697	.724	.027*
Q+	26	165	.702	.740	.038*
A	34	170	.707	.743	.036*
Q+	26	170	.702	.750	.048*
A	34	175	.702	.755	.053
Q+	26	175	.704	.755	.051
A	34	180	.698	.775	.077
Q+	26	180	.699	.758	.059

+ quenched in water

Table 5 LiF Ground in Liquid Nitrogen

Heat Treatment	% Through Sieve	Seconds in Furnace	Green Density	Final Density	Density Change
A	26	165	.723	.745	.022
A	31	165	.727	.753	.026
A	26	165	.726	.752	.026
A	31	165	.727	.758	.031
A	26	180	.723	.761	.038
A	31	180	.727	.784	.057

Table 6 Atomic Emission Spectroscopy Detection Limits

	(ppm)		(ppm)
Al	10	Hg	500
Sb	50	Mo	5
As	500	Ni	5
Ba	100	Nb	100
Be	5	Pd	10
Bi	10	P	1000
B	10	Pt	10
Cd	100	Rh	100
Ca	100	Ru	100
Cr	10	Sc	10
Co	50	Si	10
Cu	5	Ag	5
Ga	5	Na	500
Ge	5	Ta	100
Au	10	Tl	10
Hf	100	Sn	10
In	5	Ti	10
Ir	100	W	50
Fe	10	V	10
La	50	Y	100
Pb	10	Zn	100
Mg	10	Zr	10
Mn	5		

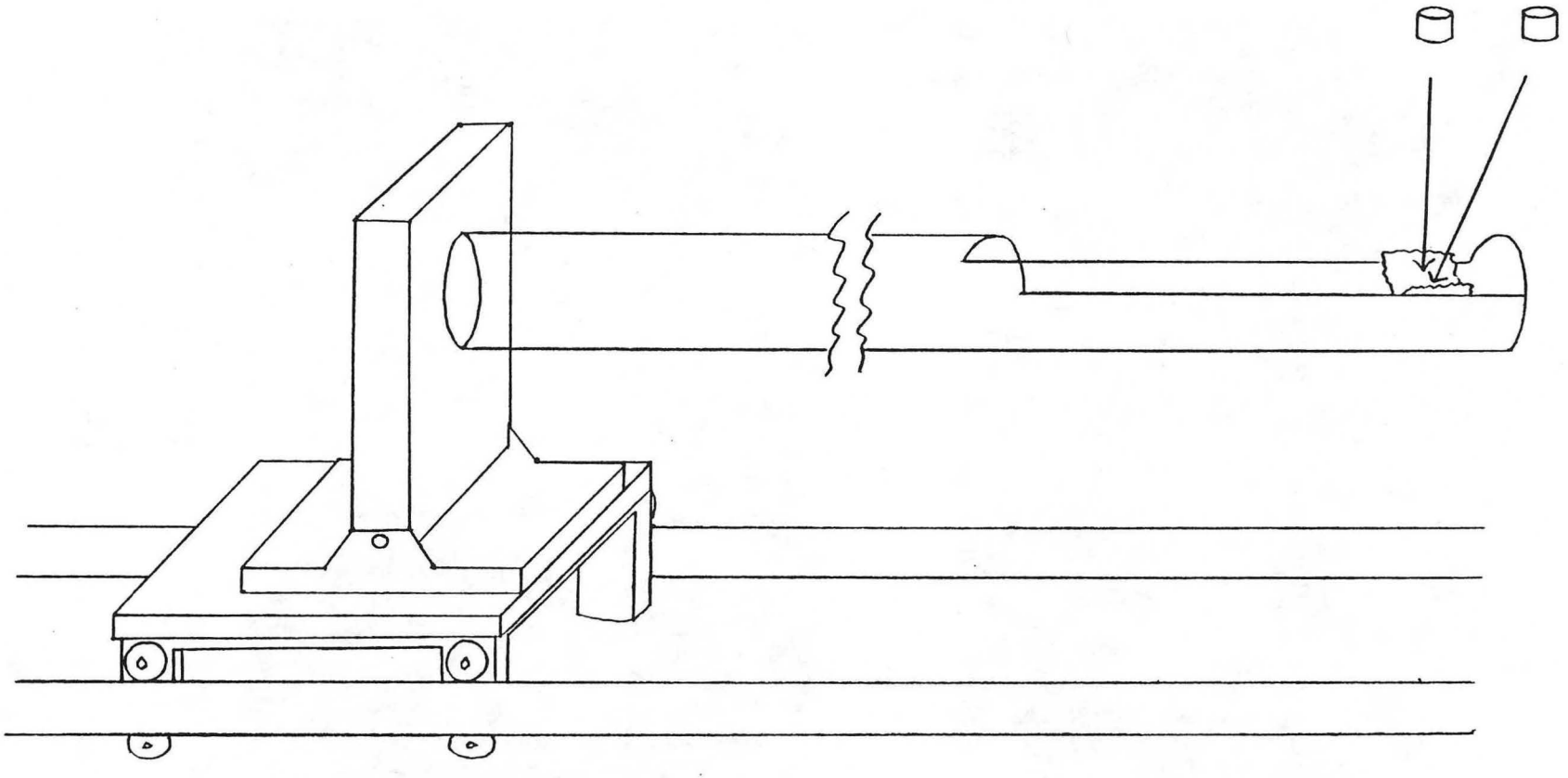

Fig. 1--a schematic drawing of the device used to place two pellets into a furnace.

Fig. 2 —— 431 μm

Fig. 3 —— 431 μm

XBB 900-9277

Figures 2 and 3--examples of surface irregularities on LiF pellets.

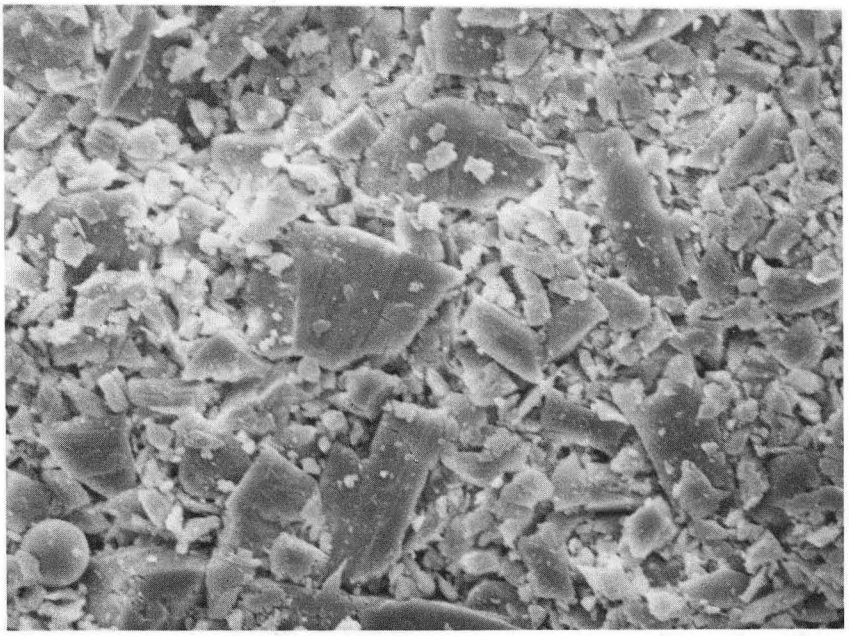

Fig. 4 —— 12.8 μm
68 % relative density

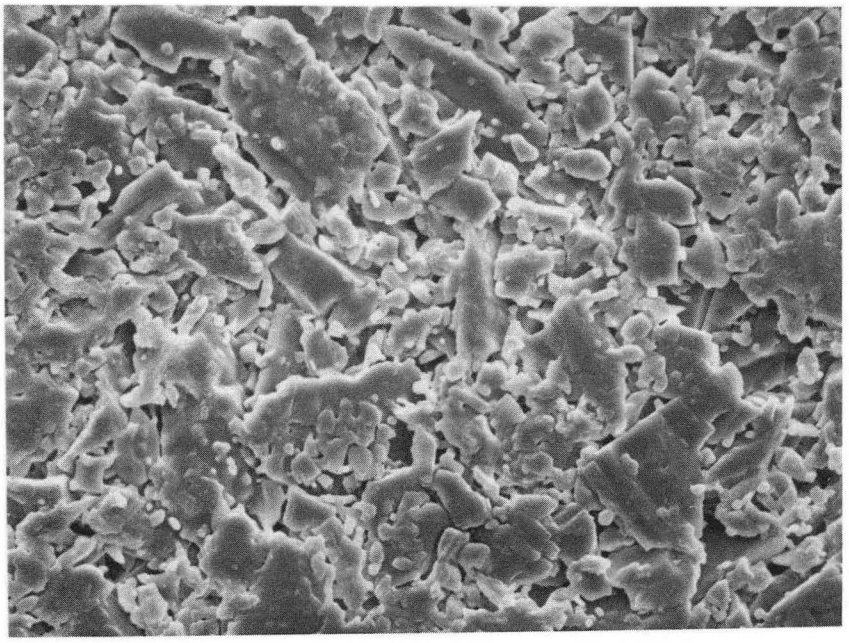

Fig. 5 —— 18.5 μm
75 % relative density

XBB 900-9278

Figures 4 and 5--typical microstructures of LiF pellets before (Fig. 3) and after (Fig. 4) fast-firing.

References

1. Unpublished work.

2. J. Golecki and C. Jaccard, "The Surface of Ice near 0 °C Studied by 100 KeV Proton Channeling," *Phys. Lett.*, **63**A (3) 374-376 (1977)

3. D. Zhu and J. G. Dash, "Surface Melting and Roughening of Adsorbed Argon Films," *Phys. Rev. Lett.*, **57** (23) 2959-2962 (1986)

4. J. W. M. Frenken and J. F. Van der Veen, "Observation of Surface Melting," *Phys. Rev. Lett.*, **54** (2) 134-137 (1985)

5. A. W. Searcy, "The Influence of Molecular Motions on the Stabilities and Shapes of Solid Particles," *J. Chem. Phys.*, **81** (5) 2489-2491 (1984)

6. C. Herring in *The Physics of Powder Metallurgy*, p.150, ed. by W. E. Kingston, McGraw-Hill Book, New York (1951)

7. P. Shewmon, *Transformations in Metals*, Ch. 3, J. Williams Book Co., Jenks, OK (1983)

8. W. D. Kingery, H. K. Bowen, D. R. Uhlman, *Introduction to Ceramics*, pp. 449-452, John Wiley & Sons, New York (1976)

9. A. Searcy, M. C. Kim, and D. Beruto, "The Kinetics of Decomposition in Powder Beds: Theory and Experiment," pp.133-142 in *Proceedings of the Symposium on High Temperature Materials Chemistry-II*, proceedings volume 83-7, ed. by Z. A. Munir and D. Cubicciotti, The Electrochemical Soc., Inc. (1983)

10. R. M. Goodman and G. A. Somorjai, "Low-Energy Electron Diffraction Studies of Surface Melting and Freezing of Lead, Bismuth, and Tin Single-Crystal Surfaces," *J. Chem. Phys.*, **52** (12) 6325-6331 (1970)

11. H. Palmour III and M. L. Huckabee, "Rate Controlled Sintering," *Proc. Int'l. Symp. On Factors in Densification and Sintering of Oxide and Non-Oxide Ceramics*, 278-297 Japan (1978)

12. H. Palmour III, M. L. Huckabee, and T. M. Hare, "Microstructural Development During Optimized Rate Controlled Sintering," *Ceramic Microstructures*, p. 176, ed. by R. M. Fulrath and J. A. Pask, Westview, Boulder, CO (1977)

13. F. Lange, "Powder Processing Science and Technology for Increased Reliability," *J. Am. Cer. Soc.*, 72 (1) 3-15 (1989)

14. M. Chu, M. N. Rahaman, and L. DeJonghe, "Effect of Heating Rate on Sintering and Coarsening," to be published in the *J. Am. Cer. Soc.* (1990)

15. M. P. Borom and M. Lee, "Effect of Heating Rate on Densification of Alumina-Titanium Carbide Composites," *Advanced Ceramic Materials*, 1 (4) 335-340 (1986)

16. T. R. Gattuso, *Quenched Lattice Defects in Potassium Chloride*, Ph.D. thesis submitted at the Massachusetts Institute of Technology (1974)

17. R. A. Menezes, *High-Temperature Dislocation Mobility in Lithium Fluoride*, Ph. D. Thesis submitted at Stanford University (1972).

18. T. G. Stoebe and P. L. Pratt, *Proc. Brit. Cer. Soc.*, 9, p. 181 (1967)

19. Data from BDH Limited, Advanced Materials Division, Poole, England (1988)

20. D. N. Seidman and R. W. Balluffi, "Sources of Thermally Generated Vacancies in Single-Crystal and Polycrystalline Gold," *Phys. Rev.*, 139 (6A) 1824-1840 (1965)

21. M. Lazaridou, C. Varotsos, K. Alexopoulos, and P. Varotsos, "Point Defect Parameters of LiF," *J. Phys. C: Solid State Phys.*, 18 3891-3895 (1985)

PART 2:

THE MORPHOLOGY OF CALCIUM OXIDE FROM CALCIUM CARBONATE DECOMPOSITION

Introduction

Previous studies[1-9], reviewed in the second section of this part of the thesis, have established the basic morphology of CaO produced by calcite ($CaCO_3$) decomposition in vacuum. When calcite is decomposed in vacuum, CaO is sometimes found in two distinguishable layers. Both layers are comprised of fairly uniformly sized, cylindrical rods on the order of 10 nm in diameter with the normal NaCl-type crystal structure. The outer layer consists of ~ $1\,\mu m$ diameter bundles of rods separated by ~ $1\,\mu m$ wide cracks. The second layer, adjacent to any undecomposed calcite--the "intermediate layer"--probably consists of rods which are relatively evenly spaced. Because sintering is negligible when calcite decomposition occurs below 700 ^{o}C in a vacuum of 10^{-3} torr or less[9,10], the outer layer is probably formed by a diffusionless, cooperative re-packing of CaO rods first formed with the uniform spacing characteristic of the intermediate layer.

The initial formation of relatively evenly spaced, 10 nm diameter CaO rods at the $CaCO_3$/CaO interface is analogous to the formation of a two solid phase eutectic structure with regularly spaced, alternating lamellae of the two phases. In the case of $CaCO_3$ decomposition, however, the phases formed are solid CaO and gaseous CO_2. The initially formed CaO rods are expected to have relatively even spacing because,

as with eutectic structures, the supersaturation necessary for growth of the separated phases is likely to be characterized by an approximately constant diffusion distance in the plane of the advancing reaction front.

The intermediate CaO layer is an unstable structure because of the strong surface interactions between the 10 nm diameter rods. The collapse of a large portion or all of the rods into the ~ 1 μm bundles of the outer layer could be caused by a chain reaction initiated by a smaller scale re-packing of rods somewhere within the intermediate layer. However, it is not clear what conditions lead to the re-packing of the rods. Powell and Searcy[9] have suggested that once the intermediate layer thickness exceeds 10 to 50 μm the rods collapse into the bundles of ~ 1 μm cross section because the maximum intermediate layer thickness they observed was 50 μm. However, the intermediate layer was often not observed at all; in these cases the outer layer was adjacent to the $CaCO_3$ crystal. This suggests that the intermediate layer is highly unstable, often transforming into the outer layer before SEM viewing. It is also possible that the insufficient resolution of the SEM or the excessive thickness of the metal coating prevented the experimenters from observing the intermediate layer.

To better understand the stability and morphology of the intermediate layer, we have conducted SEM studies of the entire cross section of partially decomposed calcite at magnifications higher than those used in previous studies. In previous high resolution SEM studies[7], only the top surface of the intermediate layer has been observed. An *in situ* transmission electron microscopic examination of calcite decomposition provided information about the CaO rod diameter and orientation, but the TEM images did not show the rod spacing and rod lengths within the intermediate and outer layers clearly.[6] We have also performed a high-resolution SEM examination of the outer

layer to confirm previous deductions (based on nitrogen condensation, mercury porosimetry,[7] and low-resolution SEM[9]) of the rod spacing or porosity within this layer.

Earlier Studies

Many techniques have been used to analyze the structure and behavior of CaO from $CaCO_3$ decomposition. Electron microscopy has revealed information about the CaO rod size and orientation, while N_2 adsorption methods and Hg porosimetry have been used to determine the surface area and porosity of the CaO. X-ray and electron diffraction have been used to determine the crystallographic orientation, identity, and reactivity of the intermediate and outer layers.

In one of the first studies of the calcite decomposition product, Glasson[1] used X-ray diffraction to analyze differences in crystal structure within the CaO. X-radiograms apparently showed that some of the CaO retained the $CaCO_3$-type lattice, and Glasson concluded that the initially formed decomposition product must be a metastable layer of CaO having a pseudo-lattice of $CaCO_3$. This conclusion supported previous predictions that a metastable decomposition product could have the pseudo-lattice of the parent crystal.[2]

A later study of a partially decomposed calcite crystal by the use of X-ray diffraction and SEM confirmed the existence of an initial metastable form of CaO, but showed it to yield a diffraction pattern different from either $CaCO_3$ or CaO.[3] The morphology of the metastable layer could not be studied because the scanning electron microscope had insufficient resolution. However, low magnification SEM examination

showed that there was an outer CaO layer with closely spaced pores of 2 μm or smaller diameter. Between the outer layer and the calcite was an intermediate layer approximately 30 μm thick having no resolvable features at × 3000 magnification. Because there was no significant volume change when calcite transformed into CaO, the total porosity of both CaO layers was estimated to be about 55 %. The pores that were observed in the outer layer did not occupy more than 30 % of the projected surface area, indicating that most of the pore volume in this layer must have been contributed by pores which were too small to see at × 3000. These conclusions are consistent with the findings of Roberts *et al.*[4], who showed that the gas-phase permeability measured in CaO aggregates from calcite crystals can be reconciled with their high surface areas if the pores have a duplex size distribution, with the larger pores being ~ 1 μm in cross section and the smaller pores being ~ 7 nm or smaller in cross section.

X-ray diffraction patterns revealed that the outer layer was polycrystalline CaO with the [110] crystallographic direction oriented preferentially normal to the exposed $(10\overline{1}1)$ plane of calcite. The intermediate layer was also found to be polycrystalline and oriented, but its only strong diffraction peak appeared at 50.3° instead of at 53.9°, the position of the (220) peak for the outer layer. From these observations, Beruto and Searcy concluded that the intermediate layer must be comprised of a metastable form of CaO, which transforms under sufficient strain to the normal crystalline form.

In a subsequent study[5], Beruto and Searcy found that the X-ray peak at 50.3° was the strongest peak of poorly crystalline $Ca(OH)_2$; the intermediate layer had reacted significantly with water vapor during exposure to air under conditions which left the outer layer as mainly unreacted CaO. They assumed that the greater reactivity of the intermediate layer compared to the outer layer indicated that the former con-

sisted of a metastable form of CaO.

In a TEM examination of calcite decomposition, Towe[6] showed that this interpretation was wrong. He performed electron imaging and diffraction as the samples were decomposing in vacuum, and thus they could not react with water vapor. He found that ~ 100 angstrom diameter CaO rods having the normal equilibrium NaCl-type crystal structure formed at the $CaO/CaCO_3$ interface; the intermediate layer did not consist of a metastable crystalline or amorphous form of CaO. Towe also found that in some areas the rods had preferred orientations (although these were not specified), and in other areas the rods were more randomly oriented. Towe did not mention otherwise distinguishable products of the calcite decomposition. In light of Towe's results, Searcy attributed the greater reactivity of the intermediate layer to a more uniform CaO rod spacing within this layer, which permitted greater access to H_2O [unpublished work].

Subsequent studies have yielded more information on the morphology of the CaO decomposition product. After having taken micrometer measurements of the volume occupied by a calcite crystal before decomposition and of the volume occupied by the CaO formed by complete decomposition of the crystal in vacuum, Beruto *et al.*[7] calculated the volumes of those pores which are $<0.1\,\mu m$ in cross section by measuring the volume of liquid N_2 taken up by the sample when the N_2 pressure reached 98 % of the saturation pressure. Since the volume of N_2 adsorbed on surfaces of larger pores is negligible, they used mercury porosimetry to obtain measurements of the volume of pores $>0.1\,\mu m$ in cross section. From these measurements they determined that the ~ 54 % total porosity in the outer layer was comprised of 42 % pores of ~ 5 nm cross section and 12 % pores of ~ $1\,\mu m$ cross section. Roughly cylindrical pores were

assumed, an assumption made plausible by the TEM observations of Towe[6] and by comparison to the N_2-adsorption isotherm. The isotherm showed the pressure dependence which DeBoer[8] identifies as characteristic of pores with cylindrical symmetry.

Beruto *et al.*[7] did not calculate the pore dimensions within the intermediate layer. However, they did obtain further evidence of its existence. Pores of $< 0.1 \mu m$ in cross section measured by liquid N_2 condensation in samples < 5 % decomposed constituted nearly 93 % of the total porosity. This indicated that the rods were more uniformly spaced than were rods within the outer layer, for which pores $< 0.1 \mu m$ in cross section constitute only ~ 78 % of the total porosity. In addition, high resolution scanning electron micrographs of the top surface of these samples showed relatively uniform diameter rods which were relatively evenly spaced, and no pores ~ $1 \mu m$ in cross section were observed. The rods tended to be aligned with their long axes parallel to the bisectors of the obtuse angles of the rhombohedral faces of the parent calcite crystal.

The intermediate layer was also observed in a study by Powell *et al.*[9], who examined cross sections of partially decomposed calcite using scanning electron microscopy. The CaO rods were not resolved at the magnifications used, but there was a distinct difference between the fracture surface morphologies of the intermediate and outer layers. The fracture surface of the intermediate layer had only a few irregularities of ~ $1 \mu m$ or higher dimensions. Powell *et al.* also noted that a smooth fracture surface would be expected for a structure with uniformly distributed aggregates of ~ 10 nm diameter rods. The outer layer had a rough fracture surface consisting of a complex pattern of ridges ~ $1 \mu m$ in cross section. This sort of pattern would be expected for a structure consisting of ~ $1 \mu m$ diameter bundles of rods separated by

~ 1 μm diameter cylindrical pores.

Some of the aforementioned studies and other studies have examined the effect of temperature, time, and/or CO_2 gas pressure on the surface area of the CaO. Using the BET method, Beruto *et al.*[10] found that the surface area of the CaO produced in vacuum at 686 °C was constant at 116 ± 4 m^2/g independent of the extent of reaction. These results implied that the transformation of the intermediate to the outer layer did not result in any significant change in surface area. In addition, X-ray diffraction measurements had shown that the CaO rod dimensions remained unchanged during decomposition at 510 °C and for up to 15 hours at that temperature after the reactions were completed.[11] Since CaO sintering was negligible in these experiments, Beruto *et al.*[10,11] concluded that the aggregation of the CaO rods into bundles probably occurred by a cooperative process rather than by diffusion.

Powell *et al.*[9] found that the CaO had a surface area of 120 ± 10 m^2/g when it was formed from *in vacuo* decomposition of large calcite crystals at temperatures below ~ 700 °C. Surface areas were lower when decomposition occurred at higher temperatures, probably because CO_2-catalyzed surface diffusion became significant as the CO_2 pressure within the pores increased with temperature, resulting in some sintering of the CaO. The higher temperatures alone were ruled out as the cause of sintering, since fully decomposed samples did not lose surface area when subsequently annealed at 900 °C for several hours in vacuum. Furthermore, previous studies had shown that CO_2 catalyzed CaO sintering. The surface area of CaO from calcite decomposition in air, which inhibits the escape of CO_2 from the pores, has been found to be much less than the surface area of CaO produced in vacuum.[1,5] It also has been shown that the sintering of CaO is negligible at 650 °C in CO_2 pressures of 0.1 torr or less, but

sintering is pronounced in CO_2 at 9 torr, near the equilibrium decomposition temperature.[12] This explains why the surface area of CaO produced in powder beds, in which the equilibrium decomposition pressure can be approached, is less than the surface area of CaO produced from individual calcite crystals.[13]

The effect of gaseous CO_2 and H_2O on pore and rod morphologies also has been investigated. After decomposing samples in CO_2 atmospheres of various pressures, Beruto *et al.*[10] made nitrogen condensation measurements of the volume of mesopores, i.e. pores with cross sections < 0.1 μm. They discovered that CO_2-catalyzed reductions in CaO surface area primarily result from a reduction in the mesopore volume. Measurements of the volume of CaO indicated that the volume of the larger pores with ~ 1 μm cross sections must increase. At high CO_2 pressures the CO_2 reacted with high-surface-area CaO to form calcite.

By exposing CaO produced from *in vacuo* calcite decomposition to high water vapor pressures at 25 °C, Beruto *et al.*[14] found that the conversion of CaO to $Ca(OH)_2$ results in lateral expansion of the rods and a reduction in pore size. X-ray diffraction was used to discover the degree of conversion of CaO to $Ca(OH)_2$ for a given time of water vapor exposure. N_2 condensation measurements indicated that the average pore size decreased after samples started reacting with water vapor, and BET measurements indicated that surface areas decreased as well. The reduction in pore size and surface area was not caused by reactions which closed off pores near the exterior of the samples; the conversion of CaO to $Ca(OH)_2$ resulted in only a small increase in the exterior dimensions of the crystals, implying that the reaction with water vapor proceeded primarily at internal surfaces of the CaO. The conclusion that the reaction occurred relatively uniformly along rod surfaces was supported by the finding that the pores still

retained their cylindrical shapes, as indicated by the shape of the adsorption isotherms. Beruto *et al.* also noted that the rods should expand because the conversion of O^{2-} planes of CaO to two OH^- planes of $Ca(OH)_2$ requires expansion in the direction normal to these planes by a factor of 1.8. This expansion was observable under the SEM after samples were exposed to the highest water vapor pressures at the longest times. Scales of $Ca(OH)_2$ were aligned into ridges parallel with the sides of the original particles. For samples exposed to lower water vapor pressures, the only SEM evidence that a large, anisotropic expansion had occurred was that occasional cracks developed in the larger particles. Beruto *et al.* suggested that cracks form because reductions in porosity introduce high levels of strain within the material.

Experimental Procedure

Calcite single crystals[a] were cleaved along their natural cleavage planes $(10\overline{1}1)$ to obtain specimens approximately 2-3 mm in height and of varying lengths and widths. One or more specimens were placed within a platinum foil basket. The basket was hung within an alumina-tube vacuum furnace, where a pressure of at most 1×10^{-4} torr at room temperature was maintained by a silicone oil diffusion pump and liquid nitrogen cold trap. The samples were heated to temperatures ranging from 620 °C to 660 °C. The thermocouple was situated within insulation adjacent to the heating coils of the furnace, and hence the temperature of the samples was not known precisely. [However, when the furnace was heated to 500 °C - 800 °C in air, and a thermocouple was placed in the center of the tube, the temperature inside the tube was found to be

a. A spectroscopic analysis is given in reference 3.

approximately 50 °C higher than the temperature of the thermocouple near the coils.] When the samples started decomposing, the pressure inside the tube increased to ~ 2-5 × 10^{-4} torr and remained at that level. After twelve to twenty-four hours had passed, the furnace was allowed to cool to room temperature. At temperatures less than ~ 200 °C, the pressure inside the tube had dropped below 1.0 × 10^{-5} torr.

After the samples had cooled to room temperature, the alumina tube was filled with N_2 gas and subsequently detached from the vacuum apparatus. To minimize reaction of the CaO with H_2O in the atmosphere, samples were then stored within a small jar containing high surface area CaO and MgO powder, which acted as a getter for water vapor. Just before SEM viewing, the samples were cleaved to expose cross sections of the partially decomposed crystals and immediately coated with gold. The thickness of the gold coating was typically about 40 nm.

One BET (nitrogen adsorption) measurement was made in order to make sure the surface areas of the CaO decomposition product were similar to those obtained in previous studies. In this case the calcite crystal was allowed to fully decompose within the furnace at a temperature of ~ 680 °C. After having cooled to room temperature, the CaO was transferred to a sample tube of a BET apparatus.[a]

a. Quantachrome Corp., Greenvale, N. Y.

Results and Discussion

Cross sections of fifteen partially decomposed calcite crystals were observed under the SEM, but the intermediate layer was found only twice. As in previous studies, the intermediate layer was distinguishable from the outer layer in part because the intermediate layer had a smooth fracture surface. The outer layer generally had a rough fracture surface, although the surface morphology of the outer layer varied greatly within each sample. Common patterns were observed in all the samples, however. The surface morphology of the outer layer probably depended primarily on the orientation of the CaO rods in relation to the fracture surface.

One example of this difference in surface morphologies within the outer layer is shown in Figures 1 and 2. Figure 1 shows the outer layer adjacent to the calcite (upper left). Both smoother and rougher patterns can be seen in the outer layer. A higher magnification view of this layer is shown in Figure 2. Here rod-shaped ridges, which appear to be about 1 μm in cross section, and cracks separating them can be seen along most of the surface. The ~ 1 μm diameter rod-shaped ridges are very similar to the ridges observed by Powell *et al.*[9], who concluded that the ridges were CaO rod bundles. However, unlike the SEM pictures of Powell *et al.*, Figure 2 also shows portions of the cylindrical pores between the rod bundles. Near the center of the picture is a portion of the surface which appears to have a finer rod-like pattern oriented in a different direction. This observation does not necessarily imply that portions of the outer layer have a different structure. It is likely that differences in surface morphology are primarily a result of differences in rod orientation and in how the surface fractured. For example, rod bundles would not be so easily visible if they fractured along their long axis.

Figure 3 shows the commonly observed pattern of a rougher section of the outer layer and an adjacent section of the outer layer comprised of fine, evenly spaced ridges. This evenly-spaced ridge pattern probably resulted from fracture parallel to the long axis of rod bundles. The wide cracks in Figure 3 could have been created when the sample was cleaved rather than during decomposition. Portions of the rod bundles are more clearly visible in Figure 4, which shows the rougher section of the same sample and an adjacent section with a fracture morphology different from the ridge pattern in Figure 3. Because of the angle of these fracture surfaces relative to the electron beam, higher magnification images could not be resolved. However, Figure 6 is a higher magnification picture of the fracture surface of a different sample that is much like the surface shown on the left side in Figure 3. The ridges and valleys in Figure 6 are probably portions of the ~ $1\,\mu m$ diameter rods and cylindrical pores. Many samples had this type of surface (e.g. Figure 5).

In some cases the ends of the rod bundles were observed (e.g. Figure 7). Cleaving the sample may have distorted their appearance or position, but they are still relatively evenly spaced. Most of the rod bundles appear to have ~ $1\,\mu m$ diameters; however, some of the rods bundles have smaller diameters, a result which will be discussed later. The different morphology in the lower right corner must result from differences in orientation of the rod bundles.

The individual rods within the outer layer could be resolved in some cases. Both the rods and portions of the rod bundles can be seen in Figures 8-10. Again, the rod bundles appear to be on the order of $1\,\mu m$ in cross section. TEM observations by Towe[6] indicate that the rods should have ~ 10 nm cross sections; however, the rods in Figure 8 are close to 100 nm in diameter, a result of the ~ 90 nm of gold coating

deposited on this sample. High-resolution pictures of the outer layer adjacent to calcite are shown in Figures 11-13. The cylindrical pore on the right side of Figure 11 has a diameter that is close to 1 μm, a value consistent with that obtained from mercury porosimetry[7] and previous SEM studies[3,9]. The CaO rods in Figures 9-13 have diameters of approximately 50 nm because the thickness of the gold coating deposited on these samples was ~ 40 nm. The lengths of the clearly visible rods are 500 - 700 nm.

In most of the partially decomposed crystals only the calcite surface and the rough surfaces characteristic of the outer layer were observed. In the two instances the intermediate layer was observed, its morphology was distinguishable from that of calcite at magnifications of 2000 × and more. Since the features of all samples could be resolved at a magnification of 2000 ×, it is unlikely that an intermediate layer could have been mistaken for calcite in any of these samples. One possible exception is the sample coated with ~ 90 nm of gold, which could have hidden the features which distinguished the intermediate layer from calcite. All the other samples, including the two in which the intermediate layer was found, had a gold coating thickness of ~ 40 - 45 nm.

The difference between the calcite and the intermediate layer surface morphologies at lower magnifications can be seen by comparing Figures 14 and 16, which show different areas of the same sample. In Figure 14 the outer layer is adjacent to calcite, and in Figure 16 the intermediate layer surface is the relatively smooth area within the center of the picture. The intermediate layer has many more cracks and a slightly rougher surface than the calcite. The intermediate layer surrounds areas with rougher surfaces, which may be areas in which the CaO rods have partially or completely collapsed into the outer layer structure. The outer layer also surrounds the intermediate

layer (see Figures 15 and 17); the intermediate layer is *not* between the outer layer and calcite. These observations suggest that rod collapse can occur locally or discontinuously within a decomposing sample, even if much of the rod collapse in the observed sample occurred after decomposition.

Some of the CaO rods within this intermediate layer could be resolved (see Figures 18 and 19). Most of the rods in both figures are 300 - 700 nm long and relatively evenly spaced. The rods appear to be preferentially oriented, although the areas in which rods or pores are not visible may consist of rods which are not oriented parallel to the surface; the ~ 40 nm thick gold coating appeared to reveal only those rods which had their long axes parallel to the surface. All of the rod diameters are larger than the expected 10 nm because of the gold coating. In addition, the gold coating probably completely covers some of the pores separating the visible rods, so that two or more rods appear as one. Unfortunately, thinner gold coatings could not be used because electron-beam charging of the sample tended to reduce the resolution even with 40 nm thick coatings. Thinner coatings of platinum and chromium were tried, but charging was an even bigger problem with these coatings (for unknown reasons).

Although most of the intermediate layer in Figures 15-19 appeared to contain mostly small, similarly sized pores, in a different sample another intermediate layer was found which contained larger pores of varying size. In this case the term "intermediate layer" is defined as any layer having a structure which is significantly different from the outer layer structure (~ 1 μm diameter rod bundles separated by ~ 1 μm diameter cylindrical pores)[a]. This definition is consistent with previous usages of the

a. Nitrogen condensation measurements[7] indicate that ~ 5 nm diameter pores also exist within the outer layer, but these pores could not be seen with the scanning electron microscope.

term, since the outer layer has been described as having a specific structure, whereas the intermediate layer simply has been described as containing more evenly spaced rods and pores which are not resolvable at lower magnifications.

Figures 20-24 show different areas of the intermediate layer with the larger pores, which are oriented perpendicular to the fracture surface. The cross sections of visible pore sizes range from ~ 20 to 200 nm, compared to a maximum pore cross section of ~ 50 nm in the other intermediate layer. Rods or rod bundles as small as ~ 50 nm in diameter can be seen in Figures 21 and 22. The faint dots in Figure 22 could be the individual rods, but they are probably islands of gold. Islands of gold were seen covering calcite in high-resolution SEM images, and these islands are also evident in Figure 19.

Figure 25 shows the smoother and darker surface of the intermediate layer surrounded by the rougher surfaces of the outer layer. The maximum thickness of this intermediate layer is ~ 80 μm. The outer layer clearly has more pores with larger cross sections (see Figures 26 and 27). Note that the shallow holes on the surface of the intermediate and outer layers in Figures 26 and 27 probably are not cross sections of cylindrical pores and may have been created when the sample was cleaved, perhaps by pull-out of rods or rod bundles. Most of the visible pores and rod bundles within the outer layer have cross sections that are smaller than 1 μm (see Figure 28). As mentioned previously, rod bundles smaller than 1 μm in diameter are also evident in the outer layer of a different sample (Figure 7). Hence, the meaning of the term "outer layer" has been expanded in this case to include any layer having a structure resembling (but not necessarily identical to) that of ~ 1 μm diameter rod bundles separated by ~ 1 μm diameter cylindrical pores.

As in the outer layer, some regions within the intermediate layer in Figures 20-27 are more porous than others (compare Figures 23 and 24). The rough surfaces within and immediately surrounding the intermediate layer in Figures 15-19 may be the surfaces of regions which are equivalent in structure to the more porous areas of the intermediate layer in Figures 20-27.

These observations of the intermediate and outer layers imply that in some areas the rods have re-packed to form the structure with the ~ 1 μm diameter cylindrical pores, and in other areas the rods have re-packed on a smaller scale or not at all. The rods are probably most evenly spaced in areas with the smallest pores. However, mercury porosimetry and nitrogen condensation measurements have shown that *fully* decomposed samples consist entirely of the structure with ~ 1 μm diameter pores.[7] The samples in these experiments had been decomposing at high temperatures for a longer period of time than the partially decomposed samples analyzed in the current study. Hence, the outer layer in Figure 28 must be an unstable structure which, if the decomposition had not been stopped, would have eventually transformed to the structure with ~ 1 μm diameter rod bundles and cylindrical pores.

One BET measurement yielded a surface area of 120 ± 10 m^2/g for a set of samples which were fully decomposed at 680 ^oC. This value of 120 m^2/g is very similar to those obtained from samples in which no sintering occurred.[9,10] Since all of the samples decomposed at temperatures below 680 ^oC, no measurable amount of sintering should have occurred in any of the samples. It is possible that in some cases hydration may have increased the rod dimensions and reduced the pore dimensions to some extent, but the thickness of the gold coating seems to account for the size of the rods seen in the SEM images.

Summary and Conclusions

Results of previous studies have implied that the intermediate layer, formed at the $CaCO_3/CaO$ interface during decomposition in vacuum, consists of relatively evenly spaced CaO rods, which eventually re-pack all at once to form a structure consisting of ~ $1\,\mu m$ diameter rod bundles separated by ~ $1\,\mu m$ diameter cylindrical pores. The results of the current study, however, indicate that the intermediate and outer layer structures and the process of rod collapse can be more complex.

Fracture surfaces often revealed portions of the ~ $1\,\mu m$ diameter rod bundles and cylindrical pores which previous studies had found comprised the outer layer structure. Some surfaces did not show this pattern so clearly, but this could have resulted primarily from the way in which the surfaces fractured. However, in two samples the ends of rod bundles were observed; many of the rod bundles and pores within the outer layer had cross sections that were less than $1\,\mu m$, although these pores were still much larger on average than those in the two intermediate layers observed. Previous studies suggest that if the calcite decomposition had not been stopped, the smaller rod bundles within this unstable outer layer structure would have eventually aggregated into ~ $1\,\mu m$ diameter bundles.

In one sample, an intermediate layer was observed which consisted of relatively evenly spaced rods, but portions of it had rough surfaces, like those of the outer layer, which are likely to be regions where the CaO rods have collapsed into bundles. In another sample, an intermediate layer consisted of regions with widely varying pore sizes. This implies that there were areas where rods had collapsed into small bundles

of varying size and other areas where no rod collapse had occurred. Unlike the findings of previous studies, both intermediate layers were not adjacent to calcite but rather surrounded by the outer layer.

The aforementioned observations show that CaO rod collapse can occur locally and on a varying scale throughout a decomposing sample. The primary difference between the structures of the intermediate and outer layers appeared to be due to the extent of rod collapse within them rather than simply whether or not it occurred. Given these new observations, the process of rod re-packing could be described as follows: rod re-packing can occur on a small scale within the intermediate layer, but a large portion or all of the rods in this layer will at some point re-pack to form the outer layer structure with much larger pores. The outer layer will either consist entirely of ~ $1\,\mu m$ diameter rod bundles or of smaller rod bundles which eventually aggregate into the ~ $1\,\mu m$ diameter bundles during decomposition or handling.

Since only two intermediate layers were found out of the fifteen samples analyzed, the intermediate layer must be a highly unstable structure; it usually transformed to the outer layer at some time before SEM viewing--perhaps during the act of cleaving the samples. The maximum thickness for the intermediate layers observed in this study was ~ $80\,\mu m$, but the maximum possible thickness of an intermediate layer could be greater within a decomposing sample not subjected to external forces which promote rod collapse.

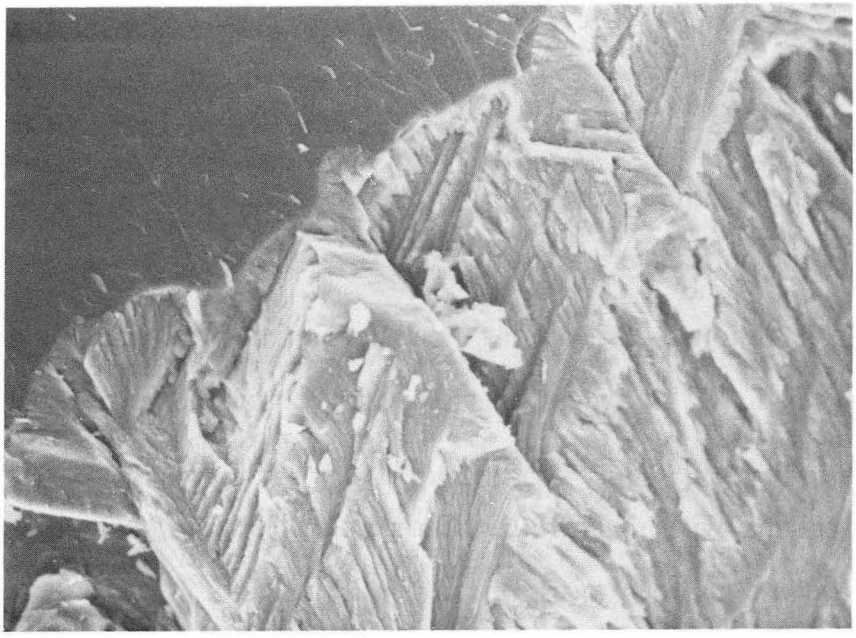

19.9 μm

Fig. 1--the outer layer is adjacent to calcite (upper left).

XBB 900-9279

3.30 μm

Fig. 2--a higher magnification view of the outer layer in Fig. 1. The ridges and cracks are portions of rod bundles and cylindrical pores.

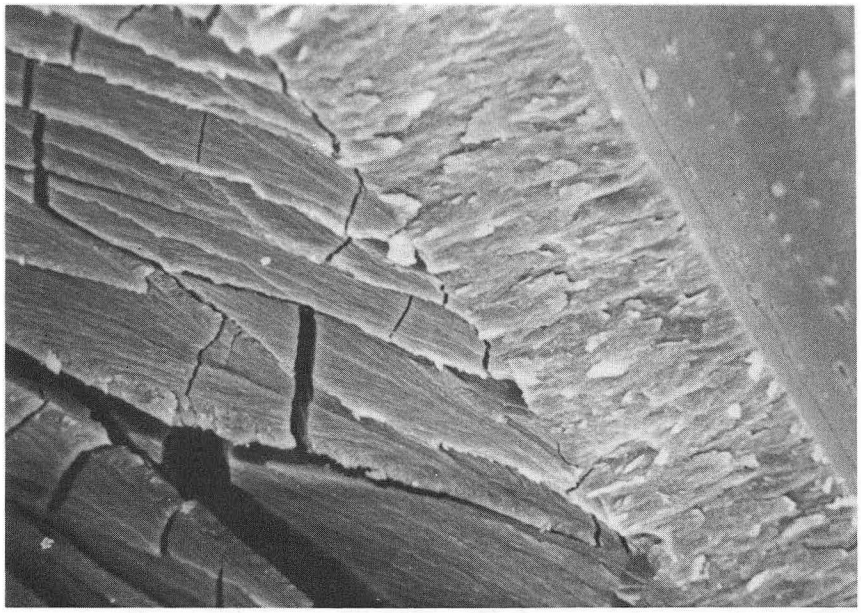

16.6 μm

Fig. 3--a portion of the outer layer near the edge of a sample. The outer layer has two different surface morphologies in this region.

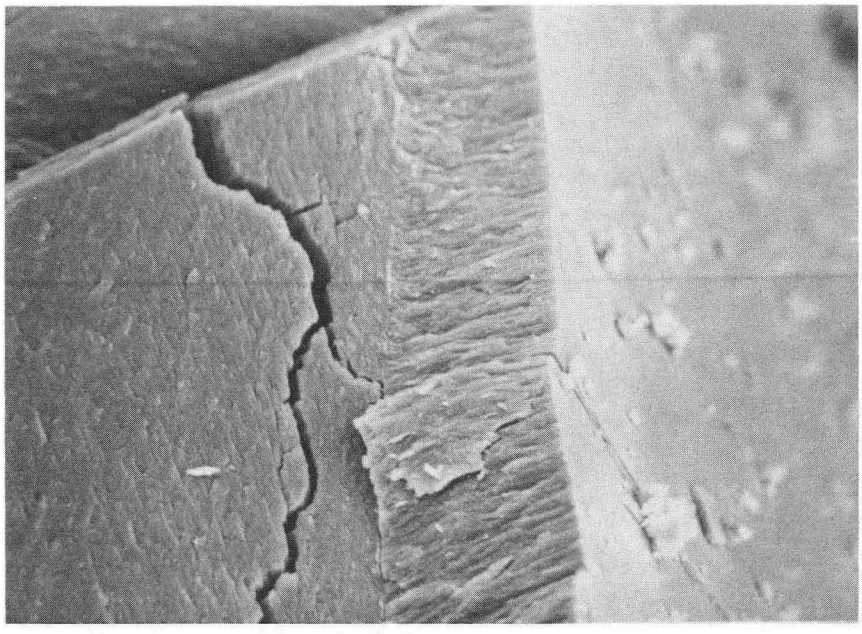

XBB 900-9280

16.6 μm

Fig. 4--a portion of the outer layer near the edge of the same sample shown in Fig. 3. Two different surface morphologies are also evident in this picture.

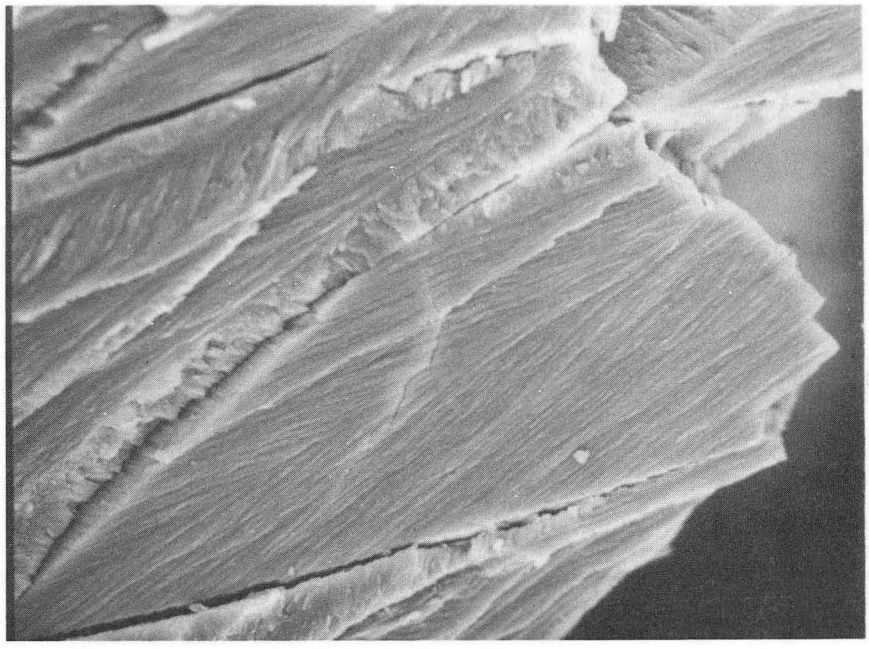

—— 9.90 μm

Fig. 5--the outer layer with rod bundles oriented parallel to the surface. Notice the similarity between the surface of this sample and the surface of the region on the left side in Fig. 3.

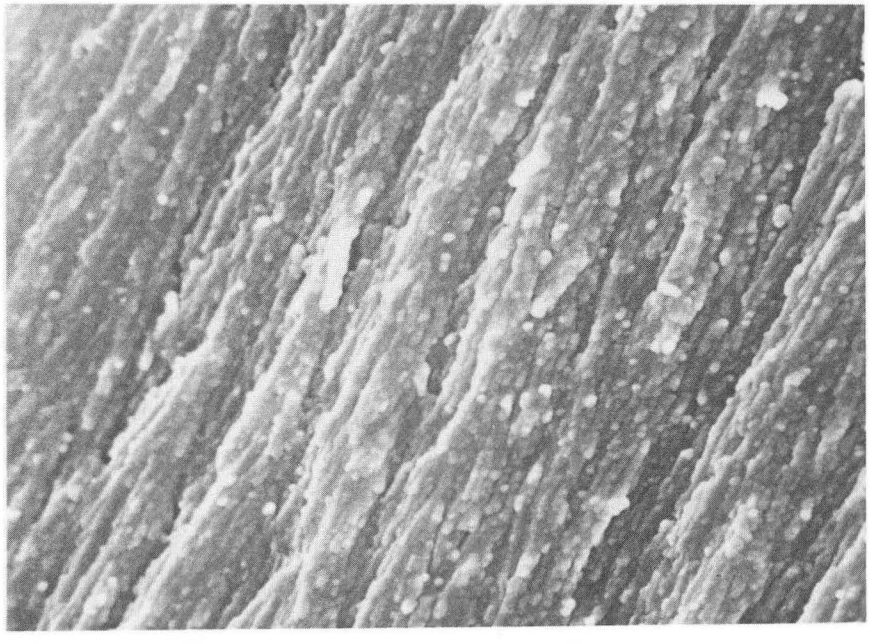

XBB 900-9281

—— 662 nm

Fig. 6--a high magnification view of the type of outer layer surface shown in Fig. 5. The ridges and valleys are portions of rod bundles and cylindrical pores.

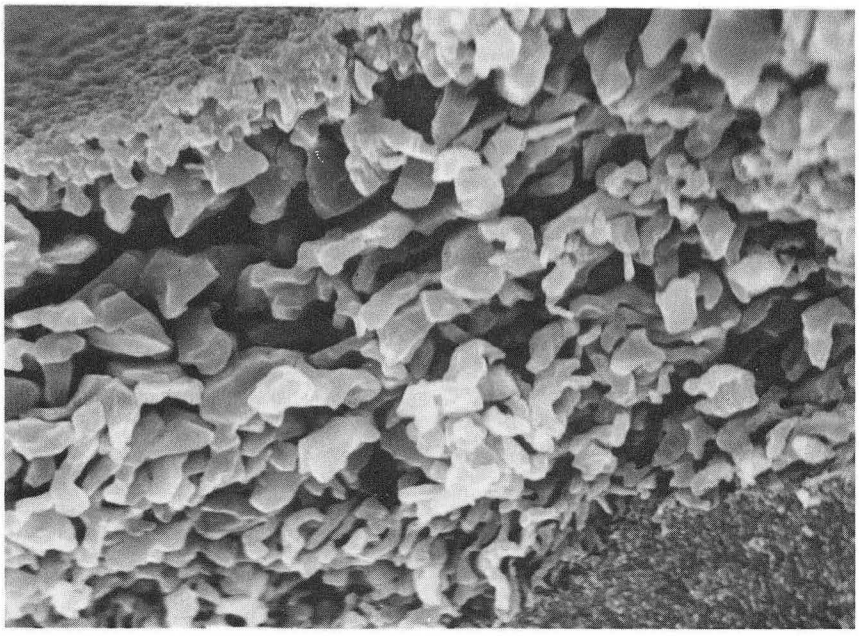

2.48 μm

Fig. 7--ends of rod bundles approximately 1 μm in diameter and less are evident within the outer layer. The region in the lower right corner must consist of rod bundles oriented in a different direction.

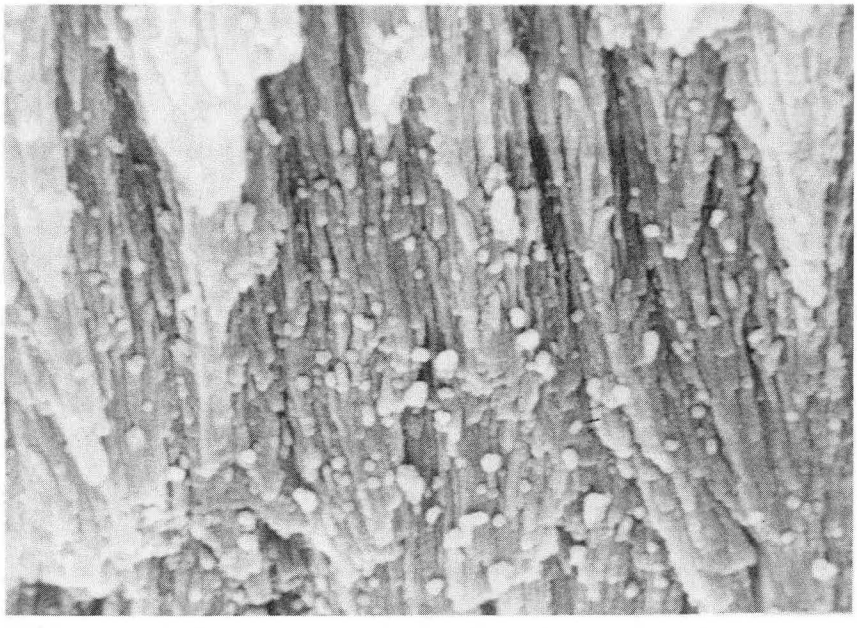

495 nm

XBB 900-9282

Fig. 8--a high magnification view of the outer layer showing the CaO rods aggregated into bundles.

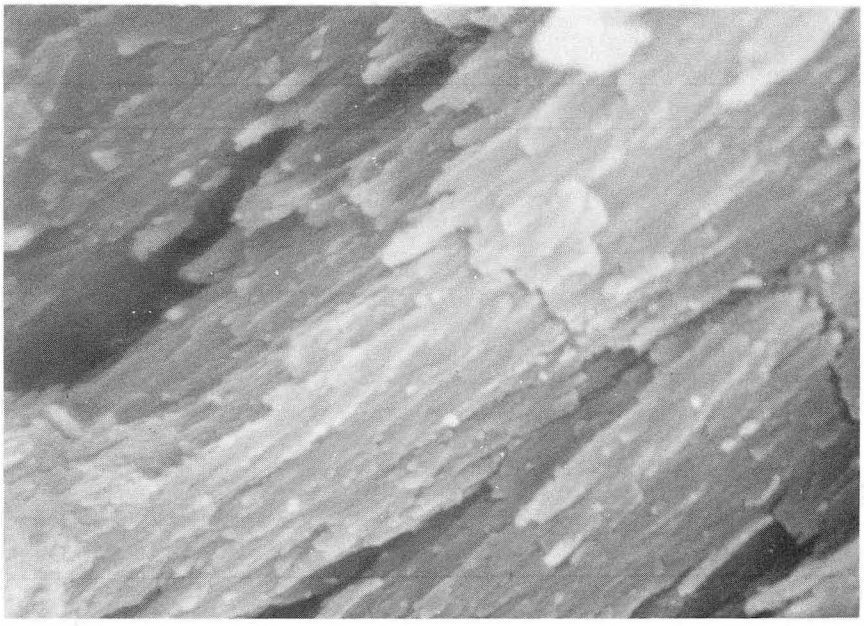

Fig. 9 —— 667 nm

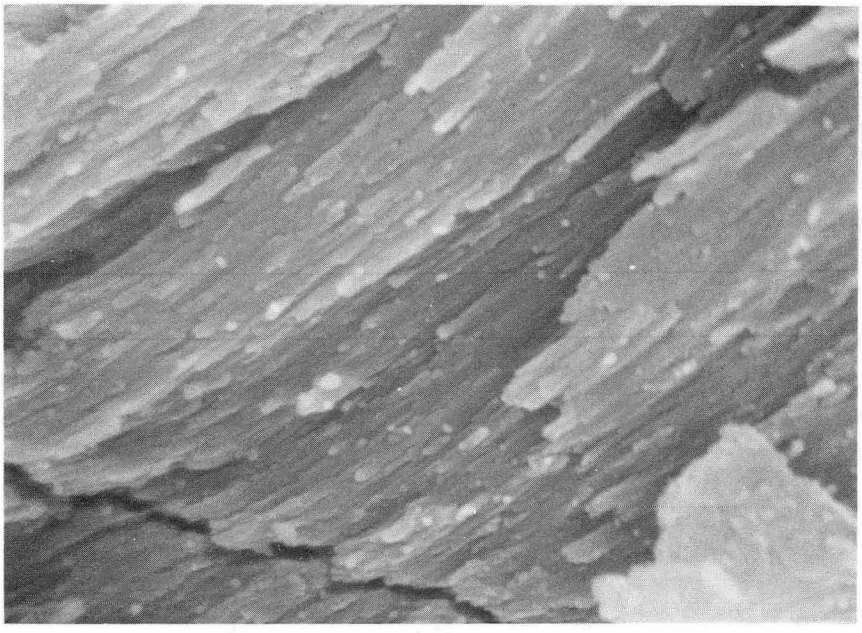

Fig. 10 —— 667 nm

XBB 900-9283

Figures 9 and 10--surfaces of the outer layer of the same sample showing CaO rods aggregated into bundles with ~ 1 μm cross sections.

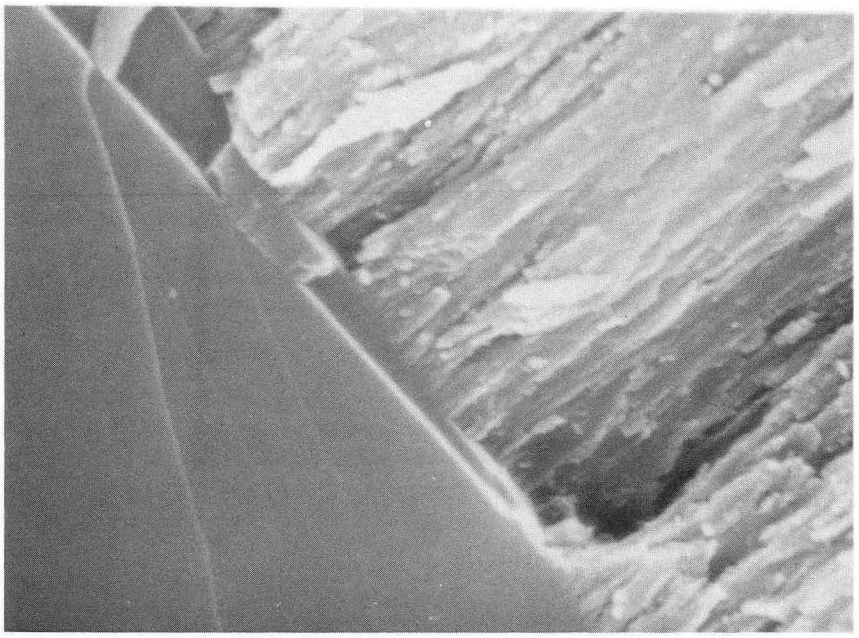

667 nm

Fig. 11--the outer layer is adjacent to calcite. Portions of cylindrical pores can be seen.

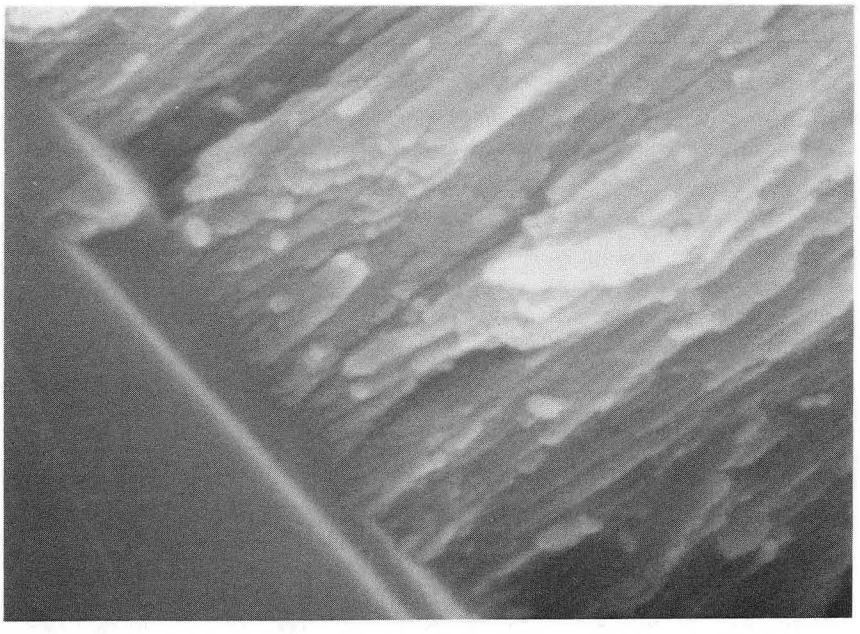

XBB 900-9284

333 nm

Fig. 12--a higher magnification view of the region in Fig. 11. The CaO rods are clearly visible.

330 nm

Fig. 13--a high contrast image of the outer layer adjacent to calcite The sample is different from that in Figures 11 and 12.

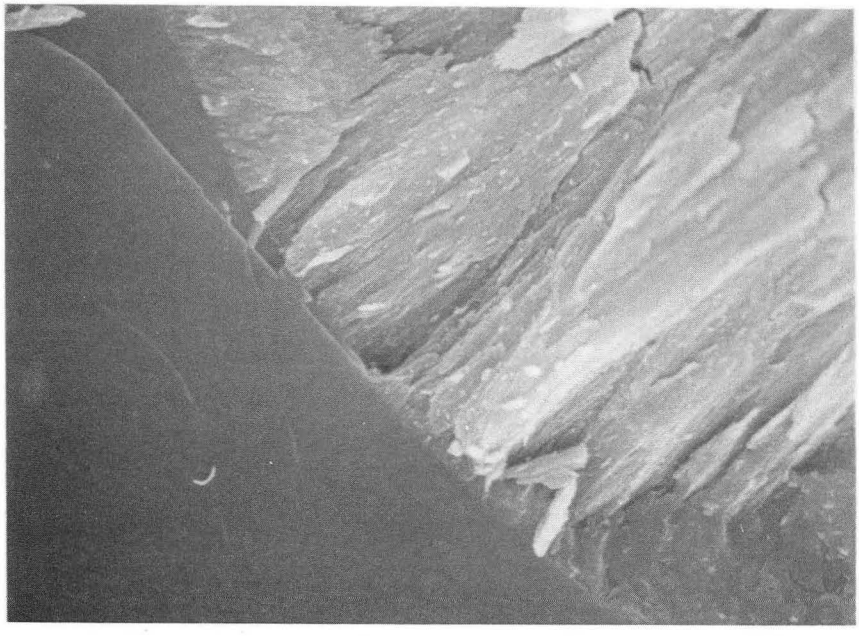

XBB 900-9285

2.50 μm

Fig. 14--the outer layer is adjacent to calcite. This picture shows the area surrounding those shown in Figures 11 and 12.

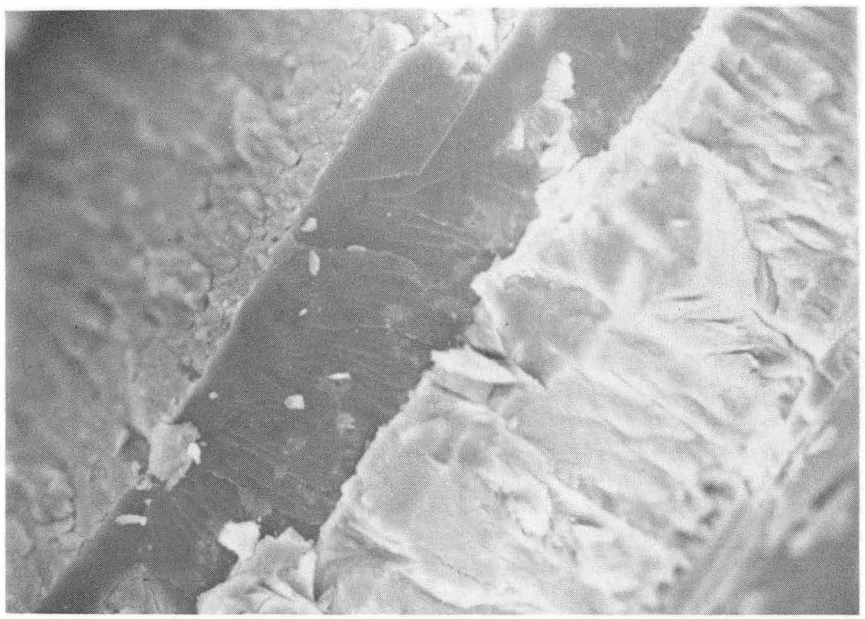

20.0 μm

Fig. 15--the smooth, darker surface of the intermediate layer is surrounded by the rougher surfaces of the outer layer.

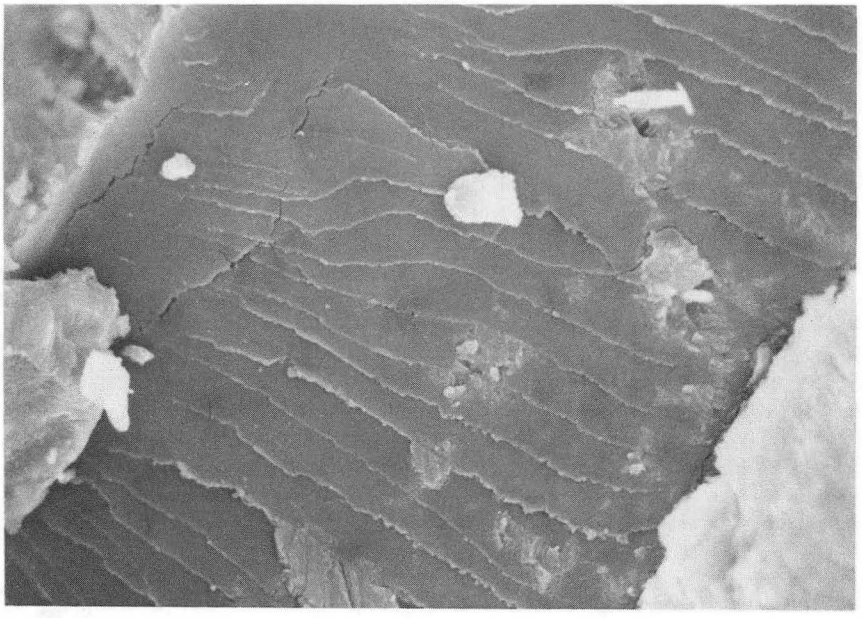

5.00 μm

XBB 900-9286

Fig. 16--a higher magnification view of the intermediate layer in Fig. 15. Cracks and islands with rough surfaces are evident within this layer.

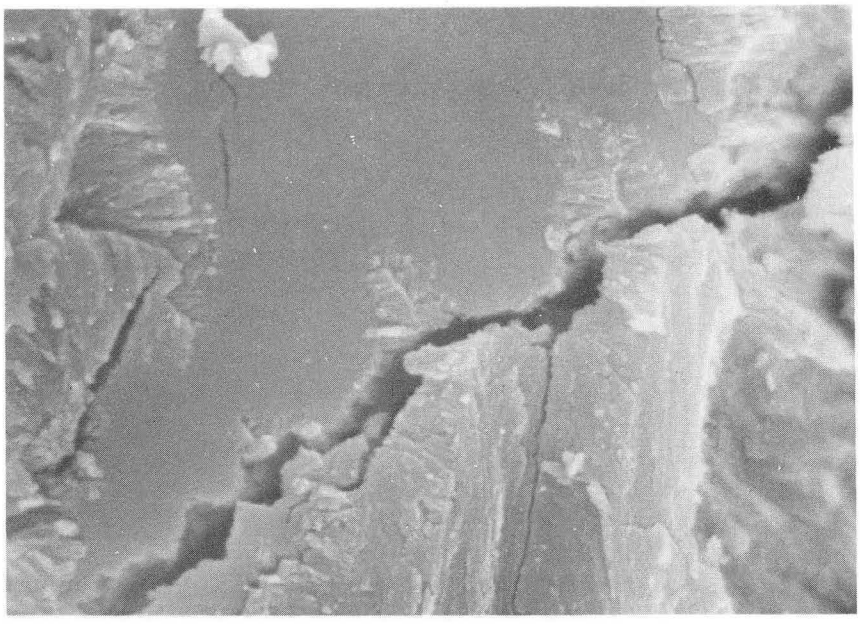

1.67 μm

Fig. 17--a different region of the intermediate layer shown in Figures 15 and 16 surrounded by regions where CaO rods have probably re-packed into bundles.

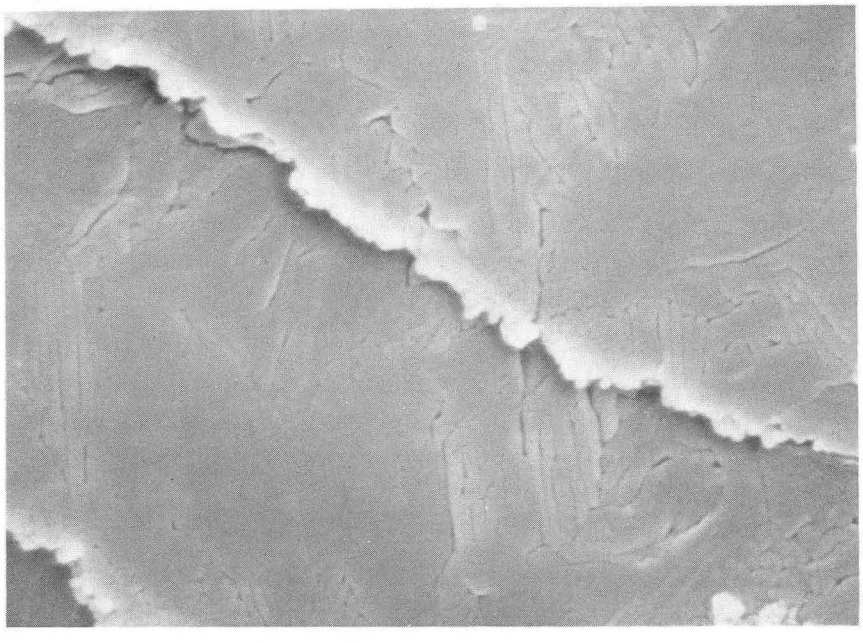

XBB 900-9287

500 nm

Fig. 18--the intermediate layer of Figures 15-17 with the visible CaO rods oriented parallel to the surface.

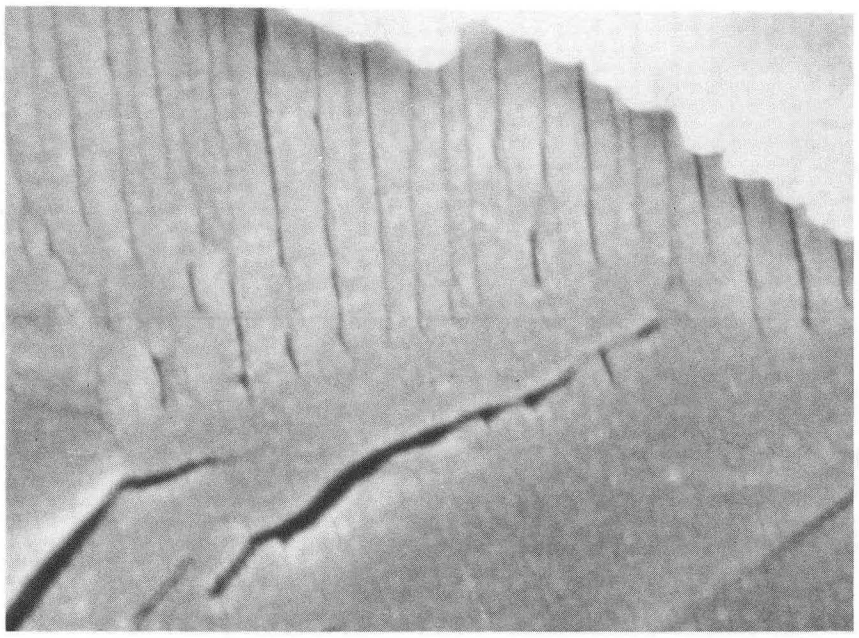

123 nm

Fig. 19--a high magnification image of the CaO rods within the same intermediate layer of previous figures. The bright area in the upper right corner is a surface at a different elevation.

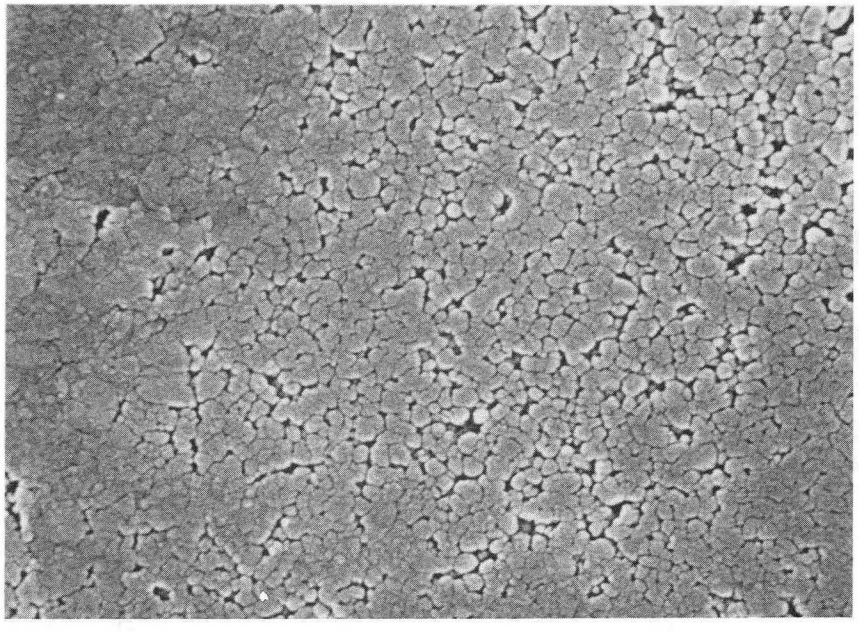

XBB 900-9288

495 nm

Fig. 20--an intermediate layer in which pores have their long axes perpendicular to the fracture surface.

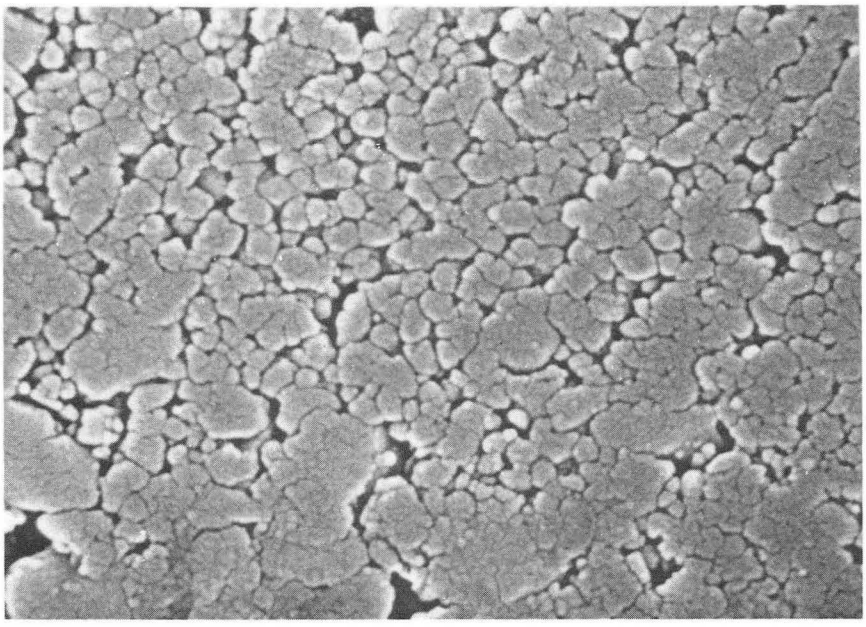

Fig. 21 —— 330 nm

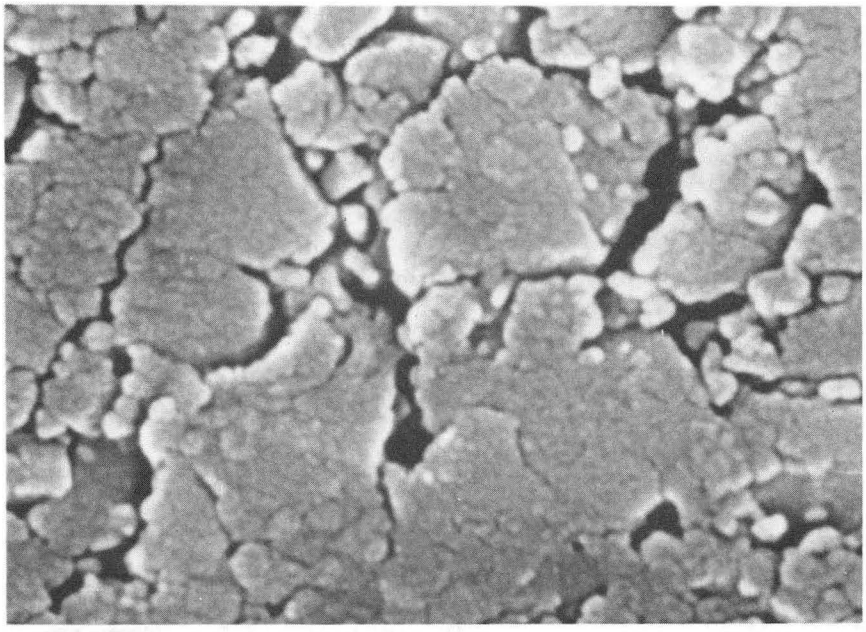

XBB 900-9289

Fig. 22 —— 199 nm

Figures 21 and 22--higher magnification pictures of a different portion of the intermediate layer shown in Fig. 20. The maximum pore cross section is ~ 200 nm.

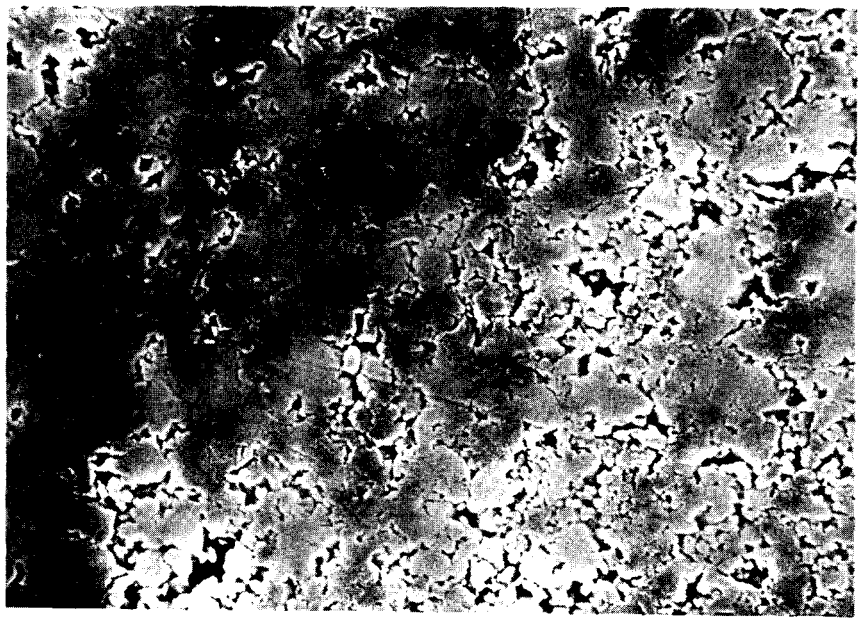

Fig. 23 —— 1.25 μm

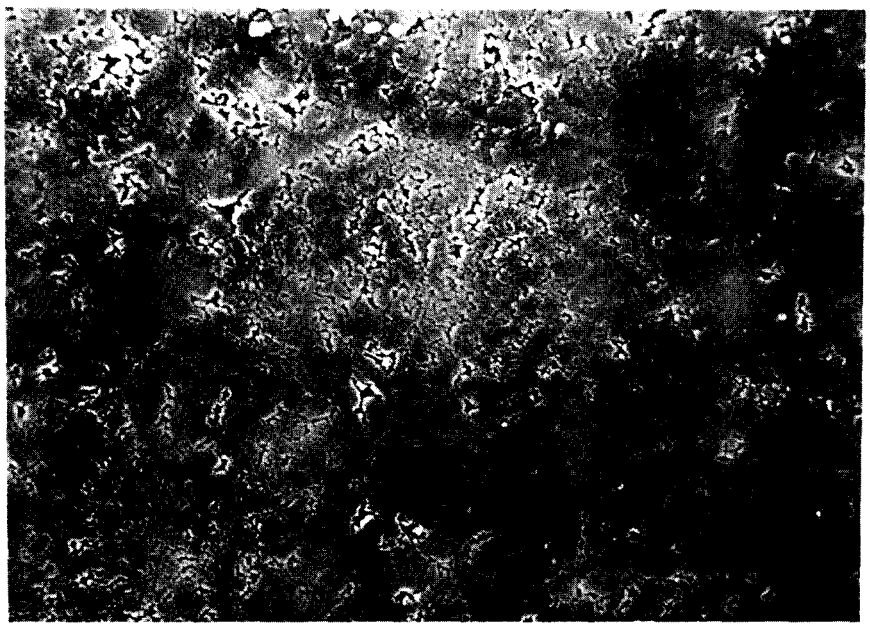

XBB 900-9290

Fig. 24 —— 1.25 μm

Figures 23 and 24--different portions of the intermediate layer shown in Figures 20-22.

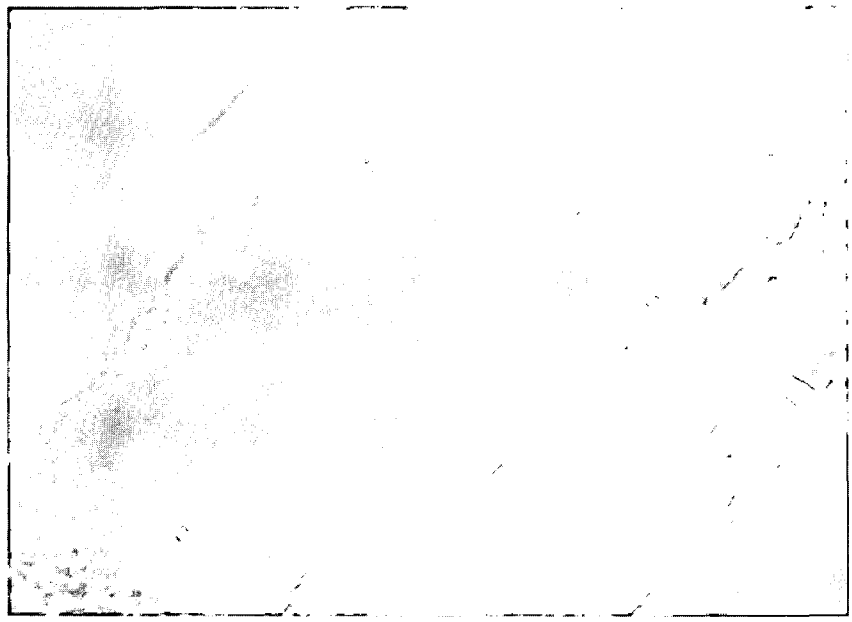

24.8 μm

Fig. 25--the smooth, darker region of the intermediate layer is surrounded by the rough surfaces of the outer layer structure. The intermediate layer shown is the same as that in Figures 20-24.

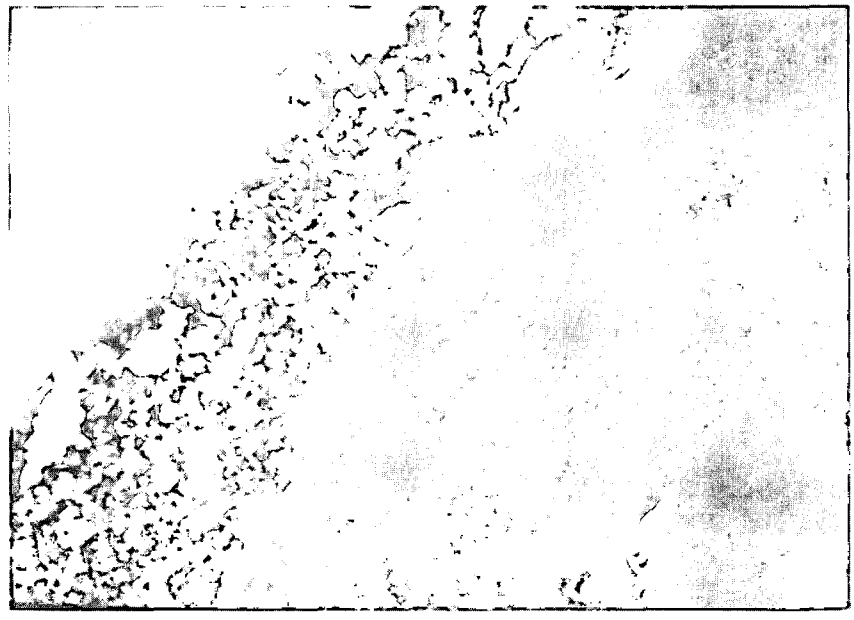

XBB 900-9291

4.95 μm

Fig. 26--a higher magnification view near the edge of the sample shown in Figure 25. The outer layer at the edge of the sample (on the left) is adjacent to the intermediate layer (on the right).

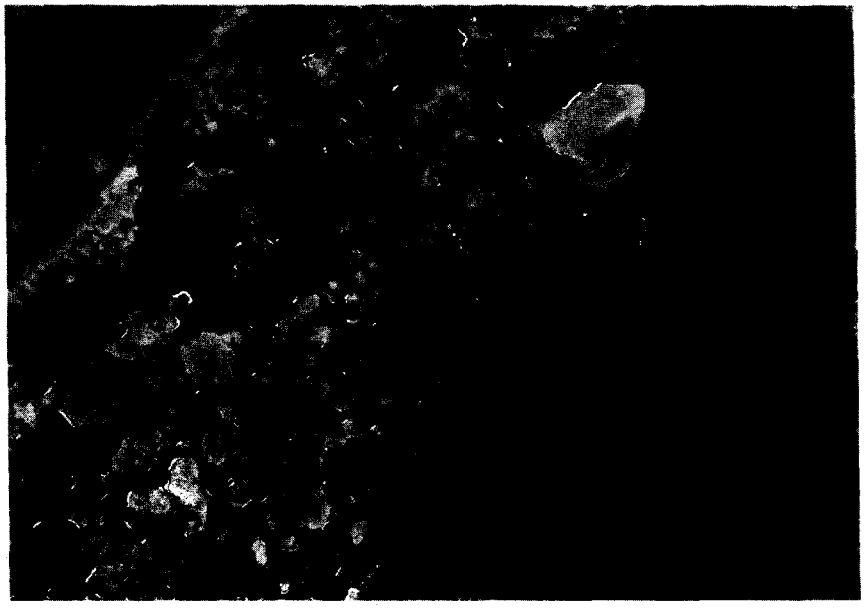

2.48 μm

Fig. 27--a higher magnification picture of the intermediate and outer layers shown in Fig. 26.

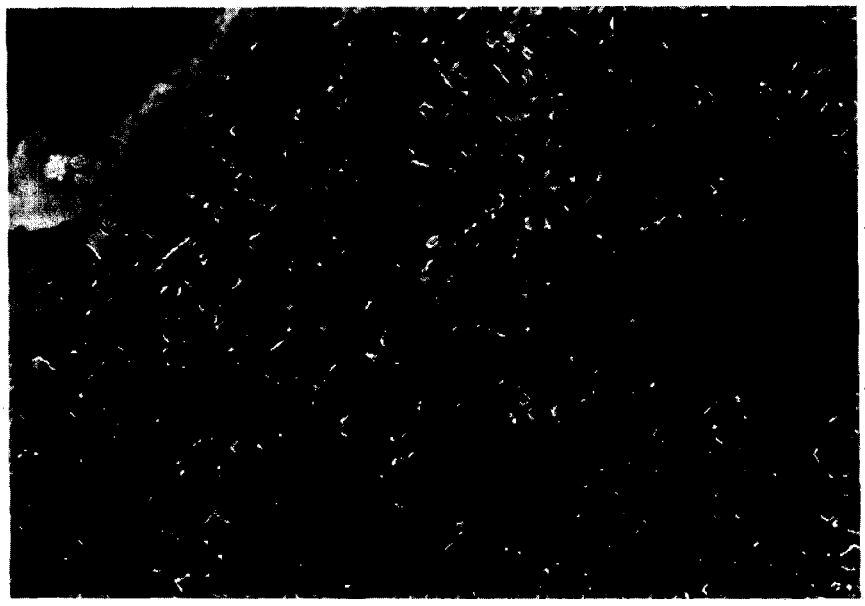

XBB 900-9292

1.66 μm

Fig. 28--a different region of the outer layer shown in Figures 26 and 27. Most of the rod bundles and pores have cross sections that are less than 1 μm.

References

1. D. R. Glasson, "Reactivity of Lime and Related Oxides: I," *J. Chem. Soc.*, **8**, 793-796 (1958)

2. S. J. Gregg, "The Production of Active Solids by Thermal Decomposition: I," *J. Chem. Soc.*, 3940-44 (1953)

3. D. Beruto and A. W. Searcy, "Use of the Langmuir Method for Kinetic Studies of Decomposition Reactions: Calcite ($CaCO_3$)," *J. Chem. Soc., Faraday Transactions, I*, **70**, 2145-53 (1974)

4. J. A. Roberts, Jr., N. S. Jacobson, and A. W. Searcy, "Kinetics of Transport of CO_2 through Porous CaO and BaO Formed by Carbonate Decomposition," *J. Chem. Phys.*, **69** (12) 5562-63 (1978)

5. D. Beruto and A. W. Searcy, "Calcium Oxides of High Reactivity," *Nature*, **263** (5574) 221-222 (1976)

6. K. M. Towe, "Ultrastructure of Calcite Decomposition *In Vacuo*," *Nature*, **274** (5668) 239-40 (1978)

7. D. Beruto, L. Barco, and A. W. Searcy, "Rearrangement of Porous CaO Aggregates During Calcite Decomposition in Vacuum," *J. Am Cer. Soc.*, **66** (12) 893-896 (1983)

8. J. H. DeBoer, *The Sturcture and Properties of Porous Materials*, pp. 68-94, Tenth Colston Symposium, ed. by D. H. Everett and F. S. Stone, Butterworths, London (1958)

9. E. Powell and A. W. Searcy, "Surface Areas and Morphologies of CaO Produced by Decomposition of Large $CaCO_3$ Crystals in Vacuum," *J. Am. Cer. Soc.*, **65** (3) C42-44 (1982)

10. D. Beruto, L. Barco, and A. W. Searcy, "CO_2-Catalyzed Surface Area and Porosity Changes in High-Surface-Area CaO Aggregates," *J. Am. Cer. Soc.*, **67** (7) 512-515 (1984)

11. D. Beruto, L. Barco, and A. W. Searcy, "Characterization of the Porous CaO Particles Formed by Decomposition of $CaCO_3$ and $Ca(OH)_2$ in Vacuum," *J. Am. Cer. Soc.*, **63** (7-8) 439-443 (1980)

12. J. Ewing, D. Beruto, and A. W. Searcy, "The Nature of CaO Produced by Calcite Powder Decomposition in Vacuum and in CO_2," *J. Am. Cer. Soc.*, **62** (11-12) 580-584 (1979)

13. A. Searcy, M. L. Kim, and D. Beruto, "The Kinetics of Decomposition in Powder Beds: Theory and Experiment," pp. 133-142, *Proc. of the Symposium on High Temperature Materials Chemistry II*, ed. by Z. A. Munir and D. Cubicciotti, vol. 83-7, The Electrochemical Soc., Inc. (1983)

14. D. Beruto, G. Belleri, and A. W. Searcy, "Vapor-Phase Hydration of Submicrometer CaO Particles," *J. Am. Cer. Soc.*, **64** (2) 74-80 (1981)

LAWRENCE BERKELEY LABORATORY
UNIVERSITY OF CALIFORNIA
INFORMATION RESOURCES DEPARTMENT
BERKELEY, CALIFORNIA 94720